DISSERTATION

REAL-TIME EROSION MEASUREMENTS OF THE HiVHAc AND SPT-70 HALL

THRUSTERS VIA CAVITY RING-DOWN SPECTROSCOPY

Submitted by

Brian Christopher Lee

Department of Physics

In partial fulfillment of the requirements

For the Degree of Doctor of Philosophy

Colorado State University

Fort Collins, Colorado

Spring 2014

Doctoral Committee:

    Advisor: Stephen R. Lundeen
    Co-Advisor: Azer P. Yalin

    Jacob L. Roberts
    David A. Krueger
    John D. Williams

ABSTRACT

REAL-TIME EROSION MEASUREMENTS OF THE HIVHAC AND SPT-70 HALL
THRUSTERS VIA CAVITY RING-DOWN SPECTROSCOPY

Electric propulsion has moved to the forefront of in-space propulsion in recent years. By making exceptionally efficient use of propellant, electric propulsion devices have significantly reduced the cost of some missions and enabled others, which had not previously been possible. Among these devices, Hall thrusters have shown particular promise. However, for many thrusters of interest, sputter erosion of the insulating channel remains a problem and continues to limit the thruster lifetime. Diagnostic tools to assess the absolute channel erosion rate rapidly remain limited. This thesis describes the use of ultraviolet cavity ring-down spectroscopy (CRDS) as a real-time diagnostic of sputtered boron atoms in the thruster plume.

Cavity ring-down spectroscopy is an ultra-sensitive laser-absorption technique which is particularly apt at measuring trace species number densities in the gas phase. In this work, ground-state atomic boron, which was sputtered from the thruster channel, was measured near 250 nm. The interrogating laser was swept across the exit plane of a Hall thruster, providing spatially-resolved boron number density measurements. Additionally, laser-induced fluorescence was used to measure the velocity of sputtered boron along the thruster axis, which were the first measurements of its kind. The measured boron number density and velocity component together provided a total boron flux from the thruster, and therefore, a channel erosion rate.

Channel erosion rates of the NASA HiVHAc and the SPT-70 Hall thrusters were measured using CRDS. Absolute erosion rates and trends with operating condition were investigated. Both thrusters were found to erode at rates proportional to the discharge power, which is consistent with the available literature. Profilometry was also used to measure the channel erosion rate of the SPT-70 thruster and revealed a factor of $\sim$5 disagreement with estimates made by CRDS.

Calcium fluoride ($CaF_2$) prism retroreflectors were developed, for the first time, as a means to improve both the bandwidth and finesse of optical cavities in the ultraviolet region. The CRDS technique used in thruster erosion measurements employed multilayer dielectric mirrors, which have relatively poor performance in the ultraviolet region. Calcium fluoride prism retroreflectors show promise to outperform the best available dieletric mirrors at 250 nm as well as provide broadband cavity operation. The design, construction, and characterization of the $CaF_2$ prisms is presented.

# Table of Contents

CHAPTER 1

# INTRODUCTION

## 1.1. OBJECTIVE

The central purpose of the work presented in this thesis is to study erosion rates of Hall thrusters using cavity ring-down spectroscopy. Hall effect thrusters are a type of electric propulsion device, which have moved to the forefront of in-space propulsion, and have enabled numerous missions not previously possible by providing very large $\Delta V$. Electric propulsion devices produce relatively low thrust due to limited on-board power and thus need to operate for thousands of hours in order to achieve the needed impulse for many missions. A problem that has long plagued Hall thrusters and limited their lifetime is the slow erosion of the insulator channel material. A thorough review of ion and Hall thrusters is given by Goebel and Katz.[1] The work in this thesis demonstrates a new diagnostic tool for real-time and non-intrusive measurement of Hall thruster erosion. In particular, erosion of the NASA High Voltage Hall Accelerator (HiVHAc) and SPT-70 thrusters were studied via cavity ring-down spectroscopy (CRDS) of sputtered boron. Absolute erosion rates as well as trends with thruster operating conditions were investigated.

In addition to measuring erosion of Hall thrusters, an objective was to improve the performance of the CRDS sensor. The CRDS sensor relies on the enhanced optical path length provided by a high-finesse optical cavity. Typically that cavity is constructed with two multilayer dielectric coating mirrors, which tend to have poor performance in the ultraviolet region. A high-finesse broadband optical cavity using calcium fluoride prism retroreflectors was constructed and characterized. Such prisms are extremely promising for improving cavity

finesse in the ultraviolet region, and therefore hold great promise to improve techniques which rely upon such cavities.

## 1.2. ELECTRIC PROPULSION

There are two drastically different regimes of propulsion for space missions: launching a payload from ground level into space and altering the trajectory of a spacecraft once it is in space. Raising a payload from ground level into orbit requires enormous amounts of energy and force, and has been exclusively achieved using high-thrust chemical propulsion rockets. At the time of writing, it cost approximately $22,000 to put one kilogram of mass into orbit around Earth.[2] There is therefore great interest in making the most efficient use of payload mass once in space. Electric propulsion devices use electric and magnetic fields to accelerate propellant to much higher exhaust velocities than are achievable with chemical propulsion.[1] Propellant exhaust velocity is a limiting factor in the achievable $\Delta$V (the maximum change in speed of the spacecraft) for a given amount of propellant. The maximum $\Delta$V is given by the rocket equation,

$$(1) \qquad \Delta V = V_e \log \left( \frac{m_0}{m_1} \right),$$

where $V_e$ is the propellant exhaust velocity, $m_0$ and $m_1$ are the initial and final rocket mass respectively. The change in payload mass ($m_0$-$m_1$) is the mass of propellant ejected. One can see from the rocket equation that for a given $\Delta$V, as the exhaust velocity is increased, the fractional change in payload mass becomes lower. Electric propulsion devices have much

higher exhaust velocities than chemical propulsion rockets, reducing the fraction of the payload occupied by propellant. For example, the current design of the asteroid retrieval mission spacecraft utilizes four 10 kW xenon Hall thrusters resulting in a total launch mass of $\sim$18 tons. To accomplish the same mission with a liquid oxygen and hydrogen chemical propulsion system would require a $\sim$225 ton launch mass.[3]

Electric propulsion was first conceived by Robert Goddard in 1906 and developed in subsequent decades.[4] To commemorate the achievement, a time capsule was sealed within the concrete floor of Clark University with the inscription,

> "The time capsule beneath this tablet is a replica of a rocket built by Robert Hutchings Goddard in 1940. Dedicated on October 12, 1966 by Vice President of the United States, Hubert Horatio Humphrey, the capsule is to be opened in the year 2466."[5]

Like many inventions, electric propulsion was independently described by Tsiolkovskiy in Russia in 1911.[6] Since that time, ion thrusters and Hall thrusters have emerged as two types of electric propulsion devices.[1] The ion thruster creates a plasma within an enclosed discharge chamber. One surface of the chamber is made of two or more closely spaced grids. Propellant ions, typically xenon, are accelerated out of the thruster by the strong electric field between the grids. The downstream plasma is then neutralized such that ions are not attracted back to the thruster and to avoid accumulating charge on the spacecraft. Figure 1.1 shows a picture of the NEXT ion thruster.

One of the several figures of merit used to describe the performance of a propulsion device is the specific impulse, $I_{sp}$.[1] $I_{sp}$ is defined as the exhaust velocity of the ejected propellant divided by the acceleration of gravity on the surface on Earth, giving units of seconds.
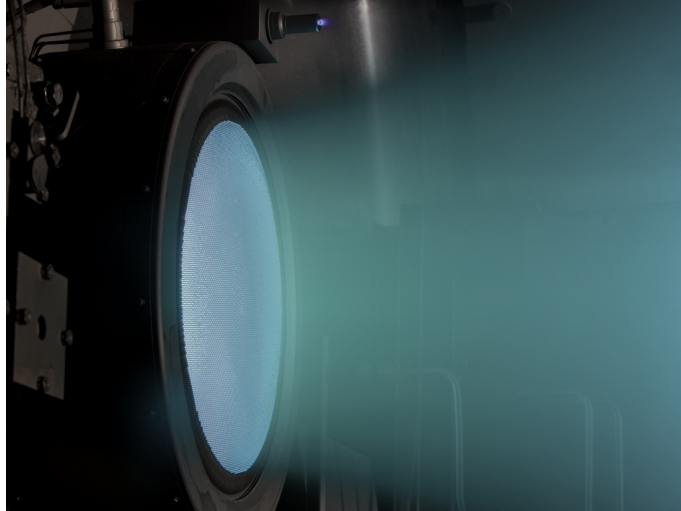
FIGURE 1.1. The operating NEXT ion thruster. Picture taken from NASA's website.[7]

Propulsion systems which rely on chemical reactions typically have specific impulses below 600 s, while ion thrusters can operate between 2000 to 10000 s and can approach efficiencies of 80% (defined as the ratio of the thrust power to the input electrical power).[1] The primary limitation of ion thrusters is the limitation in the ion current, and therefore the thrust, which can be extracted per unit area of the grids. As the potential difference between the grids is decreased, the extracted beam current will saturate due to space-charge effects between the grids.[8]

The second popular electric propulsion device is the Hall thruster. Detailed operation of the Hall thruster will be described in the next section. In contrast to an ion source, Hall thrusters create plasma within a partially open channel and do not suffer from the same space-charge limitations as in ion thrusters. Since Hall thrusters can extract larger current densities than ion thrusters, they have also achieved higher thrusts. However, their specific impulse is slightly lower at 1500 to 3000 s.[1]
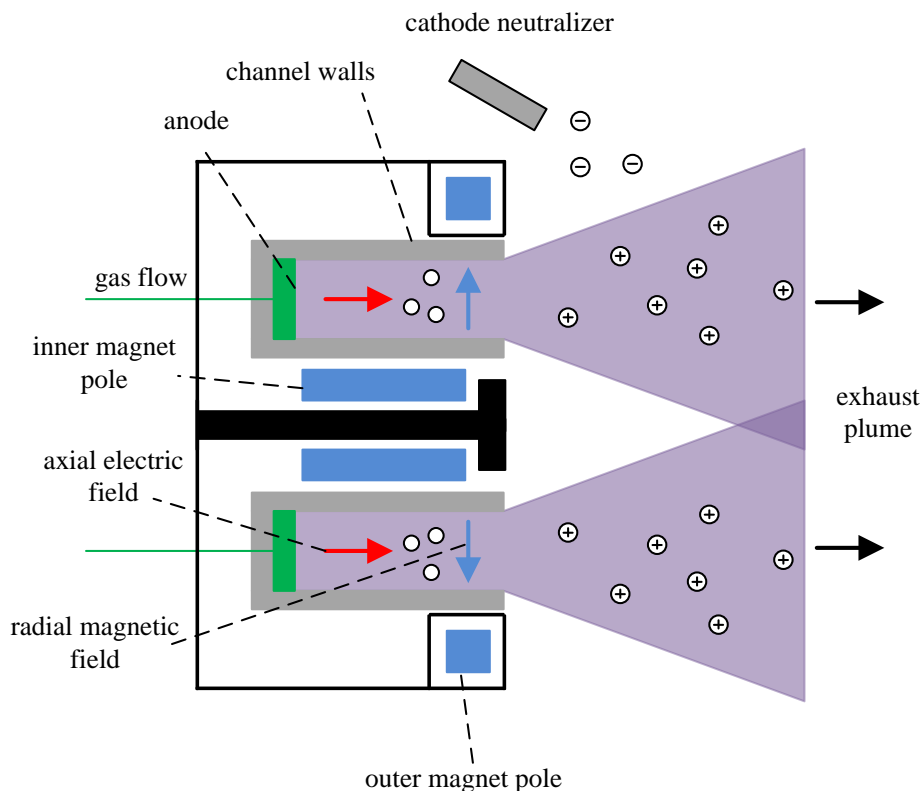
FIGURE 1.2. Operational diagram of a Hall thruster.

## 1.3. HALL THRUSTERS

Figure 1.2 shows a cross-sectional diagram of a magnetic-layer Hall thruster. A Hall thruster has a cylindrical channel with walls typically formed of ceramic materials like boron nitride or borosilicate. The anode (depicted in green) distributes the gaseous propellant, typically xenon, into the channel. The anode is held at a positive voltage ($\sim$150-600 V), creating a strong axial electric field, which will accelerate ions downstream. The reaction force to ion acceleration propels the spacecraft.[1]

The cathode neutralizer uses a low work function material to create a plasma bridge through which an electron current equal in magnitude to the ion current flows. Some of the
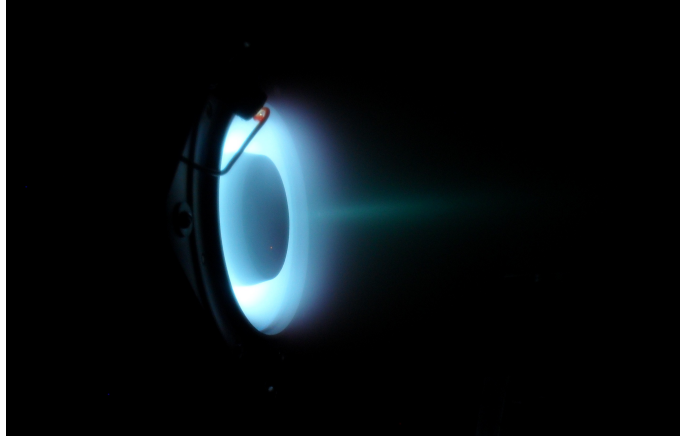
FIGURE 1.3. Picture of operating SPT-70 Hall thruster

electrons emitted by the cathode are drawn towards the anode by the axial electric field. If the electrons were allowed to stream to the anode uninhibited, then very little xenon ionization would occur. To prevent this, electromagnet coils are placed on either side of the channel, creating a radial magnetic field. The radial magnetic and axial electric fields cause the electrons to circulate around the thruster channel, creating a Hall current, from which the thruster is named. By decreasing the mobility of electrons to the anode, their path length within the channel prior to being collected at the anode is greatly increased. A longer path length in the channel increases the probability an electron will ionize a xenon atom. Electrons emitted from the cathode serve to both ionize xenon atoms and to neutralize the thruster plume. Without plume neutralization, the spacecraft would accumulate charge as it ejected ionized atoms.[1]

The thruster depicted in Fig. 1.2 is a magnetic-layer type thruster, which is in contrast to an anode-layer type thruster. Anode-layer type thrusters have shorter ionization channels and use a conducting material for the channel walls. Magnetic-layer thrusters have longer channels typically made from ceramic insulators. Nearly all Hall thrusters are magnetic-layer

type thrusters.[9] All the thrusters discussed in this work are magnetic-layer type thrusters. An operating magnetic-layer thruster is shown in Fig. 1.3

## 1.4. Sputter Erosion and Hall Thruster Lifetime

Sputter erosion is the process by which atoms are ejected from a material when bombarded by energetic particles. In many applications, sputter erosion of a material is done intentionally. For example, many optical coatings are generated by sputtering target materials onto an optical substrate.[10, 11] In electric propulsion, sputtering is an undesired side effect of creating an energetic plasma. In gridded ion sources, high energy particles can impact the grid causing sputter erosion, which in turn can lead to device failure. Ideally no particles should impact the thruster grids. However, ions can undergo charge-exchange collisions near the grids, causing them to be accelerated back towards the grids. Charge-exchange ($Xe^+ + Xe \rightarrow Xe + Xe^+$) collisions are the primary cause of grid erosion in ion thrusters.[12]

In Hall thrusters, sputter erosion occurs when high energy xenon ions impact the ceramic channel wall. Figure 1.4 illustrates the sputter erosion process in a Hall thruster. The majority of ion acceleration occurs near the channel exit in a region called the acceleration zone.[1] In the acceleration zone, the plasma is more energetic. As such, the vast majority of sputter erosion also occurs near the channel exit. The electric field created by the anode is predominantly axial and accelerates ions parallel to the channel wall. However, ions gain energy when they fall through the plasma sheath, thereby accelerating towards the channel wall.

A plasma sheath, also called a Debye or electrostatic sheath, was first described by I. Langmuir.[13] When a plasma interacts with a dielectric surface or a metal surface with
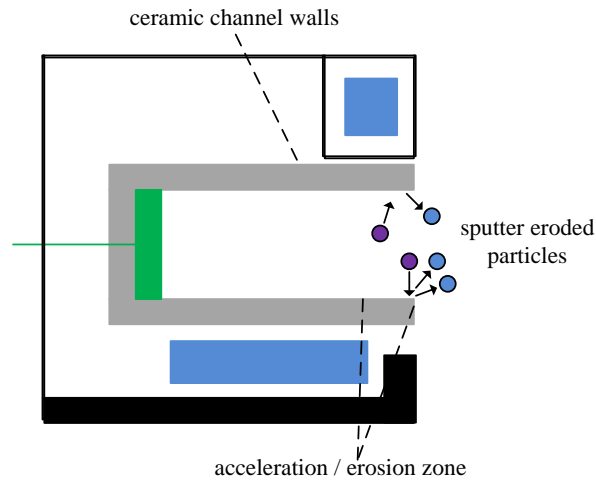
FIGURE 1.4. Diagram illustrating sputter erosion of Hall thruster channel walls. Xenon atoms (purple) impact the channel walls and cause sputter erosion, ejecting particles (blue).

floating potential, the surface will become negatively charged. Within plasmas, electrons move significantly faster than ions and will therefore flow towards surfaces at higher rates than ions. As a result, the surface becomes negatively charged and repels most electrons while attracting ions.

In Hall thrusters, the potential drop through the sheath is typically ~10-100 eV.[14] Note that sputter erosion does not occur at significant rates when the incident particle has energy below a threshold, which is a property of the material being bombarded. The threshold energy for boron nitride and related ceramics is ~40-50 eV.[15, 14] Therefore, an ion that initially has little velocity towards the channel wall can gain sufficient energy to cause sputter erosion once accelerated through the sheath.

The thruster channel walls slowly recede due to the sputter erosion process. Once the ceramic channel wall has been significantly eroded, the magnetic circuit will be exposed to the thruster plasma, causing failure of the thruster. Additionally, some of the sputtered

products from the thruster are condensable (i.e. boron). These condensable materials can adsorb on other spacecraft components, such as solar panels, altering their performance. Characterization of the sputter-erosion process is therefore critical for thruster qualification and mission design.

## 1.5. Hall Thruster Erosion Diagnostics

Accurate measurement of channel wall erosion can be difficult. Channel erosion rates of tpyical Hall thrusters are on the order of $\mu$m per hour. The current paradigm for assessing the lifetime of a Hall thruster is to perform a long duration test, preferably exceeding the length of the targeted mission, which can be many years long. For example, a BPT-4000 Hall thruster was operated for 10,400 hours as part of the flight qualification process.[16] The NEXT ion thruster currently holds the record for the longest duration life test, as it has surpassed 50,000 hours of operation.[17] Such tests are exceedingly expensive and severely limit iterative design processes. Since life test results require post-processing, they also impede the ability to study the erosion rate at different operating conditions.

Many erosion diagnostic methods have been investigated, which include profilometry[18, 19], weight loss[20–22], quartz-crystal microbalance (QCM)[23, 22], multilayer coating chip erosion[24], and optical emission spectroscopy (OES).[25–27] Profilometry and weight loss measurements require extended thruster run times for significant results and are also post facto, making parametric studies challenging. QCM techniques have the potential to provide differential sputter yields in relatively short run times, but the thruster environment gives rise to many issues with thermal stability. Multilayer coating chips, which contain tracer materials, can be installed into the thruster channel. The tracer materials are detected as layers of the chip erode with the channel wall. One of the drawbacks of such a method is

the need to specially machine and install the multilayer chip into the channel wall. Also, erosion data obtained from observing the chip erosion is highly localized to the chip location. Optical techniques are promising in that they provide real-time erosion data while being non-intrusive and not requiring alteration of the thruster. The OES technique observes spontaneous fluorescence from sputtered boron atoms in the thruster exhaust plume. OES data is obtained in real time, and is spatially resolved. However, the fluorescence signal is difficult to relate to an absolute boron concentration, since light is measured from an excited state, and collisional radiative models, or simplifying assumptions, are needed to estimate population fractions and the overall boron population[26].

Despite the work to date, there remains a need for near real-time and non-intrusive erosion diagnostics of Hall thrusters that provide information on both the absolute channel erosion rate and spatial distribution of the erosion. Cavity ring-down spectroscopy is a promising technique to achieve the aforementioned goals. Cavity ring-down spectroscopy has exploded in application in recent years.[28–31] CRDS is particularly useful in obtaining absolute trace species concentrations in gas phase. Past research has shown the possibility of measuring sputtered atoms[32, 33] including a sensor for industrial ion beam etch systems[34], and a sensor for detecting sputtered particles from an anode layer type thruster.[35] The vast majority of flight and research thrusters use insulating channels containing boron, and the sensor described in the present work allows detection of sputtered boron atoms from such thrusters. The available absorption lines from ground-state boron are limited, which led to the selection of a transition near 250 nm accessed by a frequency-quadrupled diode laser by ultraviolet continuous wave CRDS.

The first use of CRDS to measure sputtered boron from a Hall thruster was by Huang et al. at the University of Michigan in collaboration with Colorado State University[36, 37] Huang used CRDS at 250 nm to detect ground-state boron sputtered from an H6 Hall thruster. The proof of concept measurement showed the feasibility of the use of CRDS to make real-time quantitative sputtered boron measurements from an operating Hall thruster. While the measurement was largely a success, the signal to noise ratio of the resulting data was poor. Boron signals could barely be detected at many thruster operating conditions. Also, the instrument suffered from degradation due to exposure to the thruster plasma.

## 1.6. Prism Cavity-Enhanced Spectroscopy

As will be discussed later, cavity-enhanced spectroscopic techniques are lacking when compared to those in the visible or infra-red spectral regions, including detection of boron at 250 nm. Cavity-enhanced optical techniques exploit the exceptionally long path lengths which can be achieved in a high-finesse optical cavity. However, as one moves towards the ultraviolet region, the performance of dielectric mirror coatings suffers from high scatter and absorption loss, limiting the maximum cavity finesse which can be achieved. The work presented in this thesis also includes the development of a broadband high-finesse cavity using calcium fluoride prism retroreflectors. Such prisms show promise to improve both the peak finesse and spectral bandwidth of optical cavity in the ultraviolet region.

## 1.7. Thesis Overview

Chapter 2 of this thesis gives an overview of cavity ring-down spectroscopy and its use to measure sputtered boron from a Hall thruster. Previous CRDS work relevant to the presented CRDS sensor is discussed. Improvements to the performance of the sensor over previous

versions are also given. Chapter 3 describes the use of the CRDS sensor to measure channel erosion rates of the NASA HiVHAc thruster. Absolute channel erosion rates are estimated for several operating conditions, and erosion rate trends are compared to other measurements of both the HiVHAc and other thrusters. Chapter 4 presents erosion measurements of the SPT-70 Hall thruster. The absolute erosion rate was measured at the nominal operating condition and compared to profilometry measurements. Chapter 5 presents measurements of the axial speed of sputtered boron within the plume of the SPT-70 thruster using laser-induced fluorescence. The axial speed distributions are used to compute the boron flux from the thruster. Chapter 6 describes the design, construction, and characterization of calcium fluoride prism retroreflectors. Finally, conclusions are given in Chapter 7.

CHAPTER 2

# Boron Nitride Cavity Ring-Down Spectroscopy

# Sensor

Optical spectroscopy is an increasingly useful technique for non-intrusive, real-time measurement of trace species. In many applications, species concentrations are well below the limit of detection of conventional spectroscopic techniques like direct absorption spectroscopy. Even the best modulated spectroscopic sensors, which employ phase-sensitive detection and multi-pass cells with tens of meters of path length, only reach optical sensitivities of $\sim 2 \times 10^{-8}$ cm$^{-1}$ Hz$^{-1/2}$.[38] Optical sensitivity is often quoted in units of cm$^{-1}$ Hz$^{-1/2}$, which represent the absorption coefficient (cm$^{-1}$) that gives a signal to noise ratio of one for a collection time of one second. In general, the sensitivity improves (i.e. decreases) with the square root of the collection time, hence the Hz$^{-1/2}$ in the units. While such optical sensitivities may be adequate, or even superb, for many applications, it is relatively poor compared to what is needed for detection of boron within the plume of a Hall thruster. Hall thrusters often operate continuously for thousands of hours and are designed with boron containing ceramics which have very low sputter yields. As such, the rate of erosion of the boron containing channel is extremely slow and requires an optical technique with optical sensitivities of $\sim 10^{-8}$ cm$^{-1}$ Hz$^{-1/2}$ or lower.

Cavity enhanced absorption techniques have achieved optical sensitivities as low as $\sim 10^{-12}$ cm$^{-1}$ Hz$^{-1/2}$ by creating many kilometers of optical path length within a high-finesse cavity. Cavity ring-down spectroscopy (CRDS) was chosen for the boron detection

instrument because of its excellent optical sensitivity, relative immunity to laser power fluctuations, and availability of associated optical equipment. An overview of the CRDS technique is given in Sec. 2.1. The detection scheme for sputtered boron is given in Sec. 2.2. Previous iterations of the boron CRDS instrument are discussed in Sec. 2.3. Finally, the sensor's optical sensitivity was improved relative to previous versions and is explained in Sec. 2.4.

## 2.1. Cavity Ring-Down Spectroscopy Technique

Cavity ring-down spectroscopy is a direct absorption spectroscopy measurement technique that provides extremely high sensitivity by employing enhanced optical path length. The basic idea of CRDS is to measure the absorption spectrum of a sample (e.g. collection of sputtered particles) that is housed within a high-finesse optical cavity, typically formed from a pair of high-reflectivity mirrors. Figure 2.1 shows the critical elements of the CRDS boron sensor. The laser beam is injected into the optical cavity where it is reflected back and forth many times, e.g. $\sim 10^4$ passes for mirror reflectivity of R$\sim$0.9999. The intensity of trapped light inside the cavity decays exponentially with time[28–31]. In practice, one can either use a pulsed laser to inject a short pulse of light or, as is done in this work, one can build up light in the cavity with a continuous-wave (cw) laser and subsequently extinguish the laser to yield an exponential decay. An acousto-optic modulator (AOM) acts as a fast optical switch to turn off the incoming laser with a typical 90 - 10% extinction time of $\sim$100 - 200 ns. A detector placed behind the cavity measures the intensity of light exiting the cavity, which also decays exponentially, yielding the ring-down signal. The exponential decay time constant (also termed ring-down time), $\tau$, is related to the single-pass empty cavity loss $L_c$, and sample absorbance $Abs(\nu)$ by

$$(2) \qquad \frac{1}{\tau(\nu)} = \frac{c}{L}\left(L_c + Abs(\nu)\right) = \frac{1}{\tau_0} + \frac{c}{L}\int_0^d k(x,\nu)\mathrm{d}x$$

where $c$ is the speed of light, $\nu$ is the laser frequency, $l$ and $d$ are the cavity length and the sample length respectively, $x$ is the position along the optical axis, $k(x,\nu)$ is the absorption coefficient, and $\tau_0$ is the empty cavity ring-down time (often measured by detuning the laser from the sample absorption). The empty cavity loss, $L_c$, is generally dominated by mirror transmission loss and for a single-pass is then equal to 1-$R$. When the laser is tuned to resonance with the analyte, there will be additional loss due to absorption, yielding a lower ring-down time.
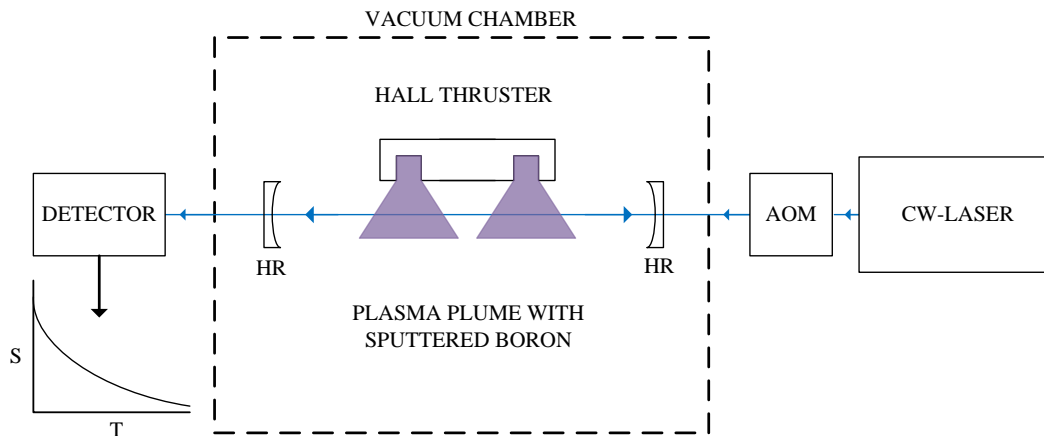


FIGURE 2.1. Schematic of a basic CRDS optical setup to measure boron in the plume of a Hall thruster. AOM:acousto-optic modulator, HR:high-reflectivity cavity mirror

A commonly used approach for finding a species concentration is to scan the laser frequency across the absorption line and to measure the frequency-integrated spectrum (i.e. the area under the spectral line). Assuming the spectroscopic line parameters are known,

the measured area, $\int Abs(\nu)d\nu$, of a transition from lower state $i$ to upper state $k$ can be readily converted to the path-integrated concentration of the lower state, $\int N_i dx$, by

$$ (3) \qquad \int N_i dx = 8\pi \frac{g_i}{g_k} \frac{v_{ki}^2}{A_{ki}c^2} \int Abs(\nu)d\nu $$

where $g_i$, $g_k$ are the level degeneracies, $\nu_{ki}$ is the transition frequency, and $A_{ki}$ is the transition Einstein A coefficient.

The laser measures the boron number density integrated along the beam. In the case of the present instrument, path-integrated boron densities are measured at various positions on a plane just past the exit plane of a Hall thruster. The measured path-integrated number densities can be deconvolved using a technique called onion-peeling to find the boron number density as a function of Hall thruster radius. In the onion-peeling technique, the erosion profile from the thruster is assumed to have azimuthal symmetry, and one divides the thruster into concentric rings with the same spacing as the path-integrated data. Figure 2.2 illustrates the onion-peeling technique. Approximately 20 to 40 'rings' were used in the work presented here. More details regarding the mathematical implementation of the onion-peeling technique can be found in Dasch.[39]
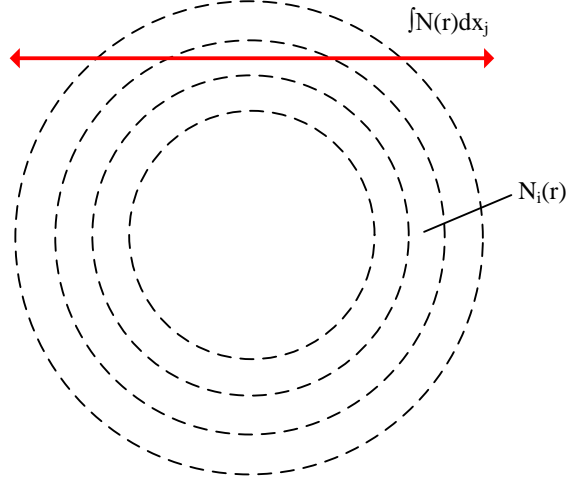
FIGURE 2.2. Schematic of the onion-peeling technique used to deconvolve path-integrated number densities. The index $j$ refers to distance of the laser relative to the thruster center, while the index $i$ refers to the radius of the ring being considered.

A matrix, $k$, then relates the path-integrated number densities, $\int N(r)dx_j$, to the number densities in each ring, $N(r)_i$, by the equation

$$(4) \qquad \sum_i k_{ij} N_i(r) = \int N(r)dx_j$$

where the elements of the matrix $k$ are the path lengths of the beam at position $p_j$ within each ring at radius $r_i$, and are given by

$$(5) \qquad k_{ij} = \begin{cases} 0, & i < j \\ 2\sqrt{r_i^2 - p_j^2}, & i = j \\ 2\sqrt{r_i^2 - p_j^2} - 2\sqrt{r_{i-1}^2 - p_j^2}. & i > j \end{cases}$$

Once the deconvolved number densities are known, the flux of boron atoms at each point along the channel is found from the product of the boron number density and velocity. Integrating the boron flux over the thruster exit area (assuming azimuthal symmetry) yields the total flux of boron atoms. As will be explained in the next section, we assume that for every boron atom ejected from the channel, one nitrogen is ejected, and no $B_xN_y$ compounds (in the case of a pure boron nitride channel). Therefore, the volumetric channel erosion rate is given by

$$\dot{V} = \frac{m_{BN}}{\rho_{BN}} \left( \frac{g_{1/2} + g_{3/2}}{g_{3/2}} \right) \Phi_{3/2} \tag{6}$$

where $m_{BN}$ is the mass of one boron and one nitrogen, $\rho_{BN}$ is the density of boron nitride, $g_{1/2}$ and $g_{3/2}$ are the level degeneracies of the two boron ground states, and $\Phi_{3/2}$ is the total boron flux in the $J=3/2$ level (i.e. boron atoms per second in the J=3/2 state).

## 2.2. DETECTION OF BORON

Our approach for detection of sputtered boron atoms from boron nitride or borosil (BN-SiO$_2$) channels is based upon CRDS absorption measurement of sputtered boron atoms. Atomic nitrogen is not a readily optically accessible species. The exact composition of the sputtered particles from boron nitride, i.e. proportions of B, N, B$_x$N$_y$ etc., is not well understood and may vary with sputtering conditions. However, detailed sputter yield measurements by Rubin et al. indicate the majority of sputtered boron is in the form of atoms.[15] Rubin et al. collected condensable sputtered products from a boron nitride target onto a witness plate and analyzed their composition with x-ray photoelectron spectroscopy. The

author's found a surface composition of ∼85% boron and ∼15% nitrogen. They assumed $N_x$ compounds did not condense on the witness plate. Based on these findings, the sputtered products are assumed to be largely as boron atoms, so each sputtered boron atom corresponds to ejection of one boron atom and one nitrogen atom (in the case of a pure boron nitride insulator) from the channel surface. It is also possible nitrogen sputters as $N_2$ or $N_x$, but this does not affect our measurements.

A partial energy level diagram for neutral boron (B I) is shown in Fig. 2.3. The ground term has two distinct levels: $2p^2 P_{1/2}$ (0 eV) and $2p^2 P_{3/2}$ (0.00189 eV). As a result, fine-structure splitting results in two distinct B I absorption lines near 250 nm: the $2p^2 P_{1/2} \rightarrow 3s^2 S_{1/2}$ transition at 249.753 nm (vacuum) and the $2p^2 P_{3/2} \rightarrow 3s^2 S_{1/2}$ transition at 249.848 nm. Based on degeneracy, 2/3 of the population will reside in the J=3/2 state. Therefore the J=3/2 ground state transition at 249.848 nm is targeted. The energy level distribution of sputtered boron in a Hall thruster plume is not well understood and may not exactly follow a Boltzmann distribution. However, the next excited state of boron is at 4.5 eV, and more than 99.9% of the population will reside in the ground state for thermalized populations at wall temperatures even into the thousands of Kelvin. Wall temperatures within an operating Hall thruster typically have maximum values of ∼600 K.[40] Further, past optical studies of sputtered metallic atoms show population distributions within fine-structure multiplets are well approximated by Boltzmann distributions.[32, 41] For these reasons, we assume all sputtered boron is in the ground state and that Boltzmann statistics can be used to relate the $2p^2 P_{3/2}$ population to the overall boron population.
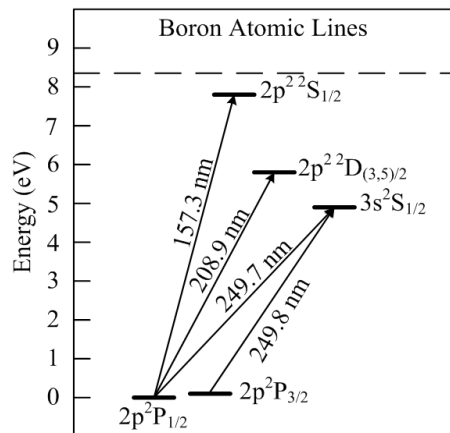
FIGURE 2.3. Partial energy level diagram of atomic boron, including the targeted transition at 249.8 nm.

There are two commonly occurring isotopes of boron: $^{11}$B (80%) and $^{10}$B (20%). There is an small difference in absorption wavelengths between the two isotopes due to hyperfine splitting and different reduced masses. However, the isotopic shift is much smaller than the Doppler broadening (typically many GHz in the plume of a Hall thruster). The laser therefore interrogates both isotopes simultaneously.

## 2.3. PAST RELEVANT CRDS WORK

The first use of CRDS to measure sputtered products, of which the author is aware, was by Booth et al.[42] Ultraviolet cavity ring-down spectroscopy was used to obtain spectra of CF, $CF_2$, AlF and $SiF_2$ in the 200 to 400 nm region using a tunable pulsed laser. The authors were able to detect species concentrations $\sim$5 times lower than what would have been possible with direct absorption spectroscopy. Shortly after, Schwabedissen et al. used pulsed CRDS at 252 nm to measure silicon atom number densities sputtered from quartz in an RF plasma.[43] Silicon number densities down to $\sim 5 \times 10^{13}$ m$^{-3}$ were readily detectable.

In 2004 Surla et al. measured various sputtered refractory metals using pulsed-CRDS in the 375-400 nm region.[33] The measurements were meant as a proof of concept for detecting sputtered products from electric propulsion devices (both gridded ion and Hall thrusters). In 2010, Yamamoto et al. developed a cw-CRDS sensor for measuring sputtered manganese atoms near 403 nm from an anode-layer Hall thruster.[35] The continuous wave sensor showed improved optical sensitivity compared to similar sensors which utilized pulsed lasers, as pulsed lasers excite multiple cavity modes simultaneously resulting in mode beating. Additionally, erosion estimates derived from the CRDS results showed good agreement with thruster mass loss measurements.

Unlike the anode-layer thruster, stationary plasma thrusters do not use metal channel walls. Boron nitride or borosil are commonly used. To target the eroded boron from such thrusters, Yamamoto et al. used a continuous-wave frequency-quadrupled diode laser near 250 nm to target the boron ground state.[44] The cw-CRDS sensor by Yamamoto et al. was the first implementation of the sensor presented in this thesis. The authors demonstrated the technique's viability by measuring sputtered boron from a planar target.

The first measurement of sputtered boron from a Hall thruster using CRDS was done by Huang et al.[36] Huang used a very similar boron detection sensor as will be presented here. Erosion rates were estimated for the 6 kW H6 Hall thruster. The technique successfully measured sputtered boron from the channel of an operating Hall thruster. Erosion rate estimates were made for a large range of operating conditions. The sensor was able to clearly resolve boron absorption signals at higher thruster powers, for which the erosion rate and boron densities are relatively high ($\sim 10^{15}$ m$^{-3}$). However, at low-power operating points, the signal to noise ratio was insufficient, and no distinct boron profile could be resolved.

There seems to have been two primary reasons for the poor signal to noise ratio. First, the optical sensitivity of the instrument was insufficient. As will be explained in the next section, the optical sensitivity of a CRDS instrument is determined from the mirror loss, the variance in measured ring-down time, and the rate at which ring downs are acquired. Mirrors reflectivities at 250 nm are relatively poor at ~99.75%, which is far below what can achieved in the visible and near infrared regions. Also, the ring-down acquisition rate was well below the theoretical limit. Second, the cavity mirror reflectivity would quickly degrade in the presence of the energetic thruster plasma, accentuating the already poor mirror performance and limiting the ability to significantly average the boron spectra.

## 2.4. Absorption Sensitivity Improvements

This section describes the work done to improve the optical sensitivity of the BN CRDS sensor over the past work described in Sec. 2.3. The optical sensitivity of a cavity ring-down instrument is given by

(7)
$$S = \frac{1}{d}\frac{(1-R)}{\sqrt{f}}\frac{\Delta\tau}{\tau}$$

where d is the path length of the laser through the analyte, $R$ is the cavity mirror reflectivity, $f$ is the number of ring downs recorded per second, $\Delta\tau$ is the $1\ \sigma$ standard deviation of an ensemble of ring down times, and $\tau$ is the average ring-down time for that ensemble. $S$ has the units of $\mathrm{cm}^{-1}\ \mathrm{Hz}^{-1/2}$. One method of interpreting such units is that $S$ is equal to the minimum detectable absorption coefficient in a 1 sec measurement time. The limit of detection then generally improves as $1/\sqrt{t}$. However, one cannot improve the limit of

detection indefinitely by continuing to average. Eventually, system drift will dominate and further averaging will increase the ensemble variance. Figure 2.4 shows a plot of sample ring-down data and its associated Allan deviation (the square root of the Allan variance) from the BN CRDS sensor. The Allan variance, also called the two-point variance, is often used to find the optimum averaging time in spectroscopic instruments.[45] As can be seen in Fig. 2.4, the minimum in the variance occurs after only a few seconds. Therefore, the laser is swept across the boron absorption feature with a period of $\sim$2 seconds such that each boron spectrum is obtained on time scales shorter than the system drift.
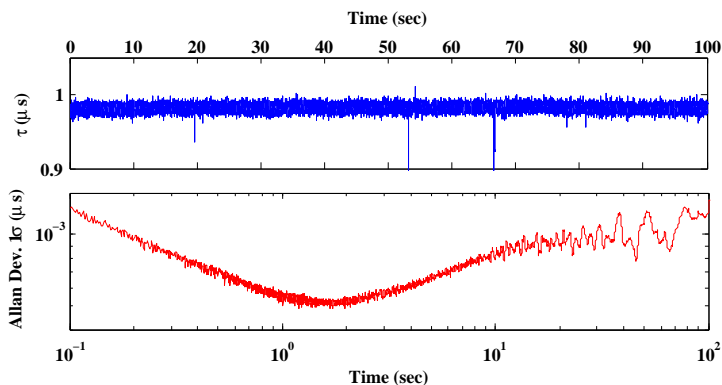


FIGURE 2.4. (Top) Measured ring-down times from the BN CRDS sensor at a constant wavelength. (Bottom) Associated Allan deviation curve showing system drift of time scales of a few seconds.

The present instrument was improved by implementing a custom AOM driver, by increasing the system acquisition rate, and by filtering ring-down times by reduced $\chi^2$. Lastly, steps were taken to mitigate the mirror degradation that occurs in the presence of an operating Hall thruster, which will be explained in Sec. 3.3. Of the mentioned systems improvements, two significantly improved the optical sensitivity: the custom AOM driver and the increased acquisition rate.

A key parameter for CRDS is the extinction ratio of the AOM.[46] The extinction ratio is the ratio of the power when the AOM is off versus on. Power may refer to either the RF

electrical power being sent to the AOM, or the optical power in the first order diffracted beam. If this ratio is not sufficiently low, residual light will continue to excite the cavity even after the AOM is off. This results in instabilities in the ring-down signal, thereby increasing $\Delta\tau$. The commercially supplied driver gave an extinction ratio in the optical power of -41 dB. The custom driver used an RF switch with significantly higher extinction ratio, resulting in an optical extinction ratio of -48 dB. While such an improvement seems small, $\frac{\Delta\tau}{\tau}$ was reduced from 0.8% to 0.4%, giving a factor of 2 improvement in $S$. By streamlining the LabVIEW control software and data acquisition hardware, the ring-down acquisition rate was increased from 150 to 600 Hz, giving another factor of ~2 improvement in $S$. The sensor presented here routinely operated with a sensitivity of $S \sim 1.0 \times 10^{-8}$ cm$^{-1}$ Hz$^{-1/2}$ which is a factor of ~5 more sensitive than previous sensor iterations. Our work improving the sensor sensitivity is outlined in a conference publication.[47]

CHAPTER 3

# HiVHAc Thruster Erosion Measurements

The High Voltage Hall Accelerator (HiVHAc) is a Hall thruster currently in development at NASA Glenn Research Center. The project is funded by the NASA Science Mission Directorate's In-Space Propulsion Technology Project to deliver a state-of-the-art thruster capable of closing various cost-capped Discovery-class missions. Mission studies have shown the 3.8 kW HiVHAc thruster can outperform state of the art 4.5 kW systems on some missions of interest.[48] The HiVHAc thruster uses a novel channel replacement mechanism which replenishes the boron nitride channel during thruster operation.[49] Prior to the work presented here, a thorough erosion characterization had not been performed. In addition to knowing the absolute boron nitride channel erosion rate, mission designers would benefit from the relative erosion rate at different thruster operating points. Such information is needed to optimize thruster throttle tables and mission flight paths.

This chapter presents real-time channel erosion measurements performed at NASA Glenn Research Center of the HiVHAc thruster using the BN CRDS sensor. The layout of the remainder of the chapter is as follows. Section 3.1 and 3.2 give the BN CRDS sensor air- and vacuum-side experimental setup respectively. Section 3.3 gives details on the counter measures used to mitigate degradation in cavity mirror performance. Section 3.4 gives the erosion measurement results and discussion.

## 3.1. Air-Side HiVHAc Experimental Setup

The description of the experimental setup is separated in two parts: the portion which resides outside the vacuum chamber (air-side) and the portion which resides inside vacuum
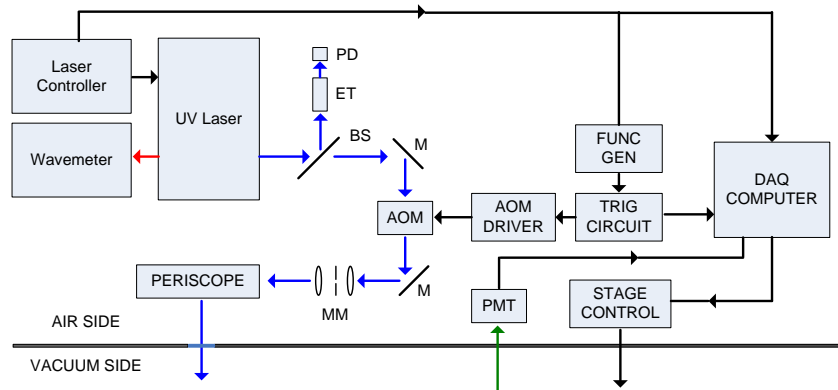
FIGURE 3.1. Diagram of the air-side CRDS experimental setup. PD: Photodiode, ET: Fused Silica Etalon, BS: Beam Splitter, M: Mirror, AOM: Acousto-optic modulator, MM: Mode-match telescope, PMT: Photomultiplier tube.

chamber (vacuum-side). Figure 3.1 shows the air-side experimental setup. The laser used was a frequency-quadrupled external-cavity diode laser (Toptica, TA-FHG110) producing about 18 mW of cw UV light, and was capable of mode-hop free scanning over an extent >75 GHz. An infrared test beam from the laser was sent into a wavemeter (Burleigh, WA-1000) which provided coarse wavelength tuning. The beam splitter directed about 10% of the primary-output power through a fused silica etalon that has finesse ~20, free-spectral range 2.2 GHz, which was used for fine frequency calibration. As the laser was scanned in a triangle wave, the transmission peaks through the etalon were counted, giving a relative frequency calibration. The remainder of the UV laser power was sent through an acousto-optic modulator (Neos, 35110-2-244-BR). The AOM acted as a fast optical switch. When the AOM driver sent RF power to the AOM, the beam was diffracted and directed towards the optical cavity. When the AOM driver was turned off, the beam was blocked from the cavity.

Ideally, the laser would be matched only to the $TEM_{0,0}$ mode of the cavity. Excitation of higher-order modes typically results in higher noise in the fitted ring-down time. Different

TEM modes have different spatial intensity distributions on the cavity mirrors. Since the reflecitvity of the cavity mirrors is not perfectly homogeneous over the surface of the mirror, different TEM modes will have slightly different ring-down times. Details of mode-matching can be found in Kogelnik and Li[50]. A telescope was specifically placed to match the beam to the fundamental cavity mode. A pinhole was placed in the middle of a mode-matching telescope, which acted as a spatial filter. A periscope sent the beam up to the height of the vacuum chamber and through an input window to the detection cavity. The light from the output fiber was detected by a photomultiplier tube (PMT, Hamamatsu, R9110).

A custom-made trigger circuit continuously monitored the signal from the PMT and compared it to the trigger level. When the signal from the cavity exceeded the trigger level, which signified a cavity resonance had been excited, the trigger circuit turned off the AOM driver and triggered the data acquisition (DAQ) computer to record the PMT signal. A function generator continuously adjusted the trigger level to account for the changing laser power as the laser scanned in frequency. When the DAQ computer was triggered, a high-speed DAQ card (Adlink, PCIe-9842) digitized the ring down at a rate of $10^8$ samples/sec. A sample ring-down signal and associated exponential fit are shown in Fig. 3.2. At the same time, a slow DAQ card recorded the laser frequency. Each digitized ring down was fit to an exponential. The ring-down time and its associated laser frequency form the function $\tau(\nu)$ from Eqn. 2. After recording a given number of ring-down events, the DAQ computer moved the thruster stage in order to record erosion at a different position on the thruster.

## 3.2. Vacuum-Side HiVHAc Experimental Setup

The HiVHAc thruster was operated in NASA Glenn's VF8 facility, which is an entirely oil diffusion pumped chamber with a 1.5 m diameter and 5.5 m length. Figure 3.3 shows a
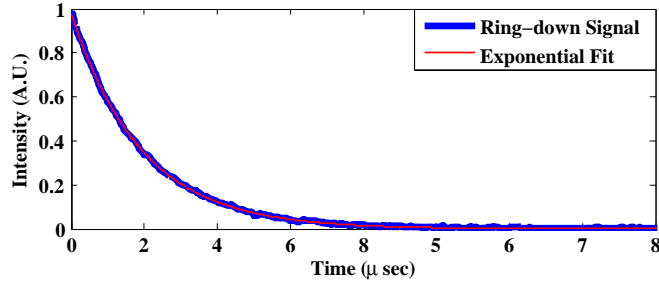
FIGURE 3.2. Sample ring-down signal (blue) and associated exponential fit (red).

picture of the HiVHAc thruster and the optical support structure within VF8. The chamber base pressure was $\sim 4 \times 10^{-7}$ Torr. With 41 standard $\text{cm}^3/\text{min}$ (sccm) of Xe flowing (a nominal anode flowrate), the background pressure was $\sim 1 \times 10^{-5}$ Torr (corrected for Xe). The thruster was mounted onto a vertical motorized translation stage, allowing boron spectra to be obtained at different positions along the thruster exit plane. Throughout this paper, the relative position of the thruster and laser beam will be reported in the non-dimensional $P$ unit. When path-integrated boron densities are reported, the non-dimensional beam position is used, and refers to the location of the laser beam relative to the thruster. The solid blue line in Fig. 3.4 corresponds to $P=0$, i.e. where the laser beam is tangent to the inner channel wall. The dashed blue line shows the $P=1$ coordinate, where the laser is tangent to the outer channel wall. When absolute boron densities are reported, the non-dimensional coordinate refers to the thruster radius. A radius of $R=0$ is the radius of the inner channel wall, while $R=1$ is the radius of the outer channel wall. Note that in this system coordinate, the thruster center has a negative value.

Figure 3.4 shows a diagram of the vacuum-side experimental setup. The interrogating laser beam entered through the chamber window from the right of the figure and was centered on the back surface of the first cavity mirror. A 54 cm long optical cavity was formed by a pair of high reflective mirrors (R=99.75%, MLD Technologies). The axis of the cavity was
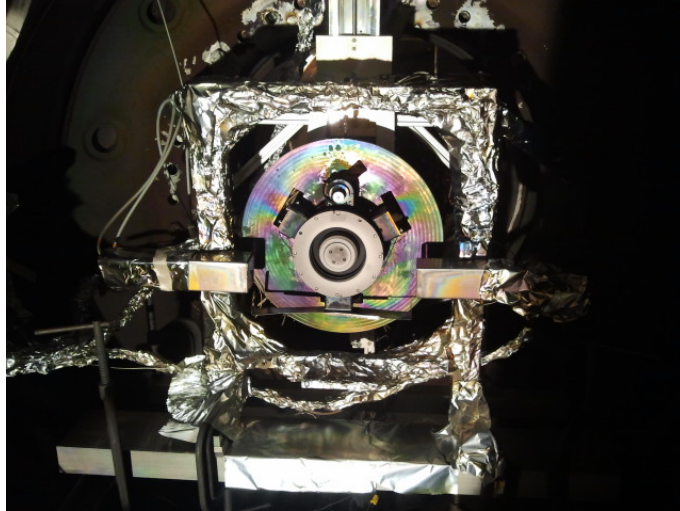
FIGURE 3.3. Picture of the HiVHAc thruster and CRDS setup within the VF8 chamber. The optical frame was wrapped in 3 layers of foil to help reduce misalignment induced by heating.

parallel to the exit plane of the thruster, and was 6 mm downstream from the exit. Each mirror was placed on an optical mount, allowing for fine adjustment of the mirrors. The first cavity mirror mount has two motorized actuators, allowing for cavity adjustment while under vacuum. Light exiting the optical cavity was focused into a 500 $\mu$m diameter core fiber for detection using an off axis parabolic mirror.
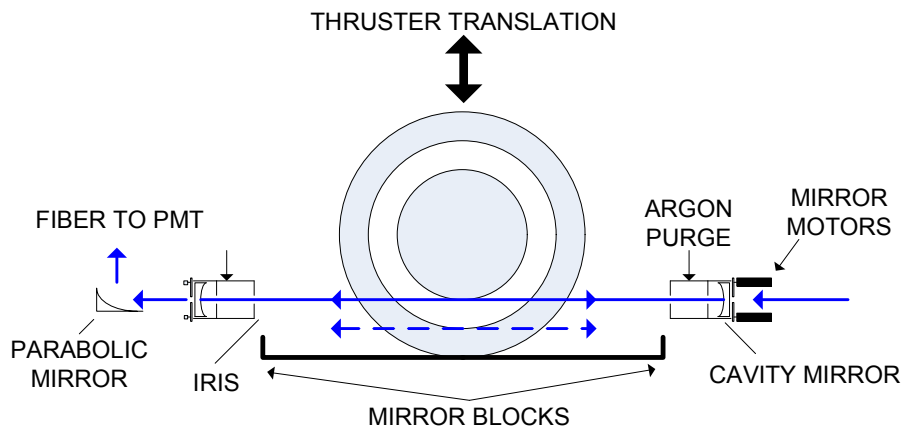


FIGURE 3.4. Diagram of the vacuum-side optical setup. The two cavity mirrors form the high-finesse optical cavity, with the optical axis 6 mm downstream of the thruster exit plane. The solid line corresponds to a beam position of P=0, while the dashed line corresponds to P=1.

In front of each mirror were two 3 mm diameter irises for the laser to pass through. The mirrors were sealed off from the thruster plasma with the exception of the two holes for the beam. Exposure to the thruster plasma causes degradation in the mirror performance. The irises served to block as much plasma exposure as possible. Additionally, a 1 sccm argon purge flow was introduced in front of each mirror. The purge flow acted to mitigate degradation in mirror reflectivity due to exposure to the thruster plasma, the details of which are given in the next section. The argon filled the volume in front of the mirrors, creating a region with a mean free path of ~1 cm, which served to deflect sputtered particles from streaming directly to the mirror surfaces and coating the mirrors. Two mirrors covers were attached to the translation stage. While the thruster was operating, but the optical sensor was not being used, the thruster was translated up, and the mirror covers blocked the irises, thereby minimizing the mirror degradation during thruster bake out (waiting for the discharge current to stabilize as water evaporated out of the channel ceramic). The thruster was operated for over 11 hrs, resulting in the mirrors degrading from 99.82% reflectivity to 99.55%, corresponding to a factor of ~2.5 drop in optical sensitivity.

### 3.3. Mirror Degradation Counter Measures

The plasma environment near a Hall thruster is harsh, particularly for optics. As the thruster operates, the effective reflectivity of the cavity mirrors slowly decreases, resulting in poorer boron detection sensitivity. The degradation appears to have two causes: sputtered particle deposition and damage from vacuum ultraviolet light. Sputtered particles, either from the thruster itself or back sputtering from the vacuum chamber, can adsorb to the mirror surfaces, reducing their reflectivity. Also, the xenon plasma in the thruster plume emits UV light with photon energies well in excess of the 250 nm probing laser. These high energy

photons can create defects in the multilayer mirror coating, also reducing its reflectivity. Similar degradation has been observed when dielectric coated mirrors were irradiated with a pulsed UV laser.[51] Once the thruster was turned off, the mirror reflectivity would recover approximately 1/3 of the lost reflectivity over the course of a few hours.

Unmitigated, the mirror reflectivity degrades to the point of being ineffective within a matter of minutes. By including the mitigation steps below, the degradation rate of the cavity loss was held below 20% per hour, allowing ample time for CRDS data collection. Also note that the mirrors can be blocked while the thruster continues to run, stopping the degradation.

Each mirror was housed inside a 2.5 inch long lens tube, with 3 mm diameter irises placed 0.5 and 2 inches downstream (see Fig. 3.4). The irises allowed the laser beam to reach the mirrors, but significantly reduced the exposure to the thruster plasma. Additionally, a 1 sccm argon purge flow was introduced in front of each mirror, which created a mean free path of ∼1 cm and increased the background chamber pressure with the thruster running by less than 5%. Particles which entered the irises had a high probability of colliding with an argon atom, and therefore a high probability of being deflected from streaming directly to the mirror surface. The top curve in Fig. 3.5 shows the collision probability of an incoming particle as a function of purge flow rate. A collision cross section was estimated assuming a hard-sphere collision between a carbon atom (selected because a graphite beam dump is used) and an argon atom. The pressure within the purge volume was found by calculating the needed pressure drop across the iris in order to have an equilibrium in particle flow. From the collision cross section and pressure, a mean free path is found, giving a characteristic length over which particles will stream into the purge volume. In red, the change in chamber

background pressure resulting from the purge flow is plotted as a function of purge flow rate. The facility pumping speed was assumed to be 10,000 L/s, which is the pumping capacity of the Colorado State University facility, while NASA's VF-8 facility has a ~10 times higher capacity.
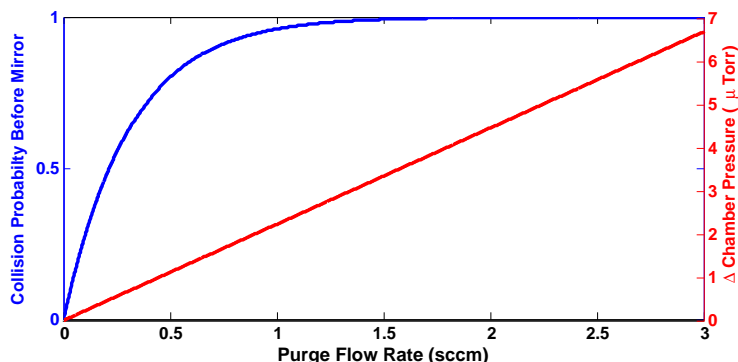


FIGURE 3.5. (Left axis, top curve) Probability an incoming particle collides with an argon atom as a function of purge flow rate and (right axis, bottom curve) the resulting chamber pressure increase from the purge flow with a facility pumping speed of 10,000 L/s.

### 3.4. EROSION MEASUREMENT RESULTS AND DISCUSSION

Figure 3.6 shows representative boron absorption spectra at different channel locations with the thruster running at 500 V discharge voltage and 2 kW discharge power. The laser frequency was continuously swept across the boron resonance. The horizontal axis gives the relative laser frequency (i.e. the 0 point is arbitrary). In this particular case, the center of the boron resonance was near 0.4 cm$^{-1}$. The 250 nm laser could not scan sufficiently far in frequency to capture the entire spectrum. In order to differentiate between empty-cavity loss and boron absorption, it is necessary to capture both the center of the absorption peak and one side of the baseline. For this reason, the center of the laser scan was intentionally offset from the center of the boron resonance. For each spectrum, 5,000 ring-downs were recorded.
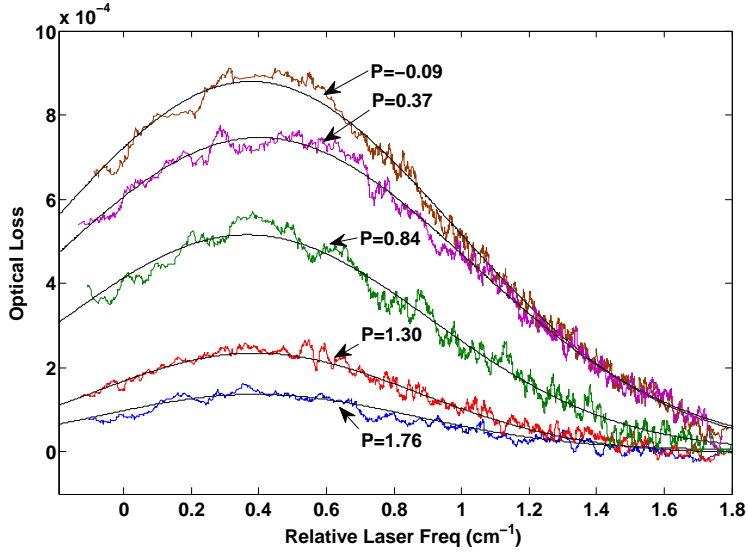
FIGURE 3.6. Representative boron absorption spectra for the 2 kW, 500 V thruster condition. The different spectra are at different positions along the thruster channel (i.e. different $P$ coordinate). The black lines are Gaussian fits.

Although the spectral broadening was entirely due to Doppler shifting, there was no reason to assume a Gaussian velocity distribution, as the boron population may not have undergone sufficient collisions to thermalize. Nevertheless, a Gaussian fits the data very well, and was used to compute the total area under the spectral curve (the value $\int Abs(\nu)\mathrm{d}\nu$). Equation 3 then yields the path-integrated boron density (i.e. the integral of the boron density along the laser path). The largest path-integrated values are seen near $P=0$, where the laser is tangent to the inner channel wall. As expected, the values decrease when the laser was moved away from the channel (i.e. $P > 1$).

Figure 3.7 shows the path-integrated boron number densities as a function of channel position. The thruster was held at 500 V, while the power was set at 1, 1.5, 2, 2.5 and 3 kW. At each setpoint, data was not taken until the discharge current had stabilized (constant to within $\sim$1% over a few minutes).
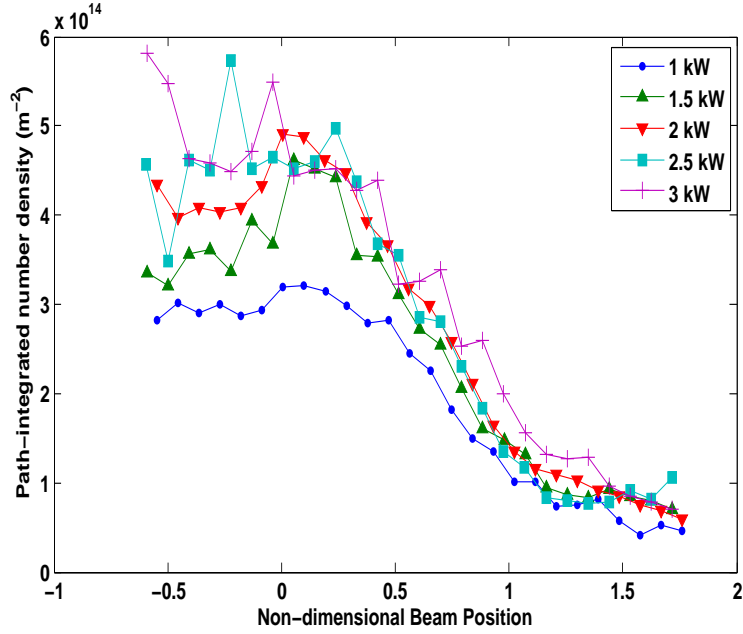
FIGURE 3.7. Path-integrated boron number densities as a function of channel position. The thruster was held at 500 V for each condition.

Figure 3.8 gives the same information as Fig. 3.7, except that the power was held at 2 kW, while the discharge voltage was varied.
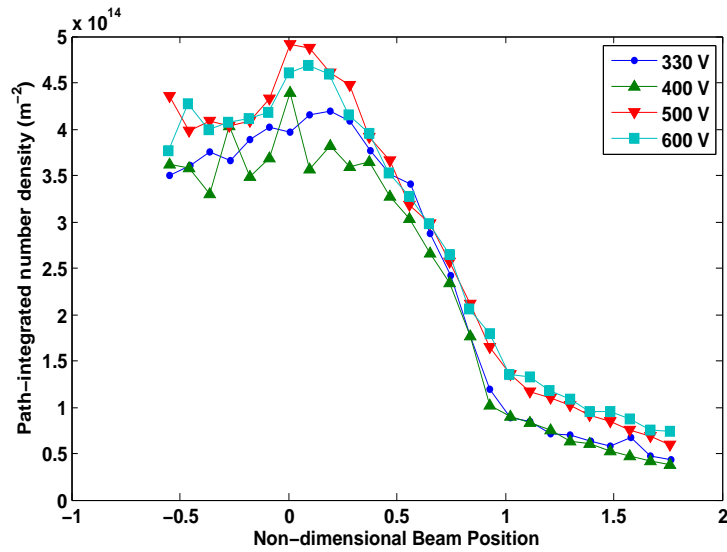


FIGURE 3.8. Path-integrated boron number densities as a function of channel position. The thruster was held at 2 kW for each condition.

The sensor showed good repeatability. The 2 kW, 500 V thruster condition was measured at the beginning and end of testing and is shown in Fig. 3.9.
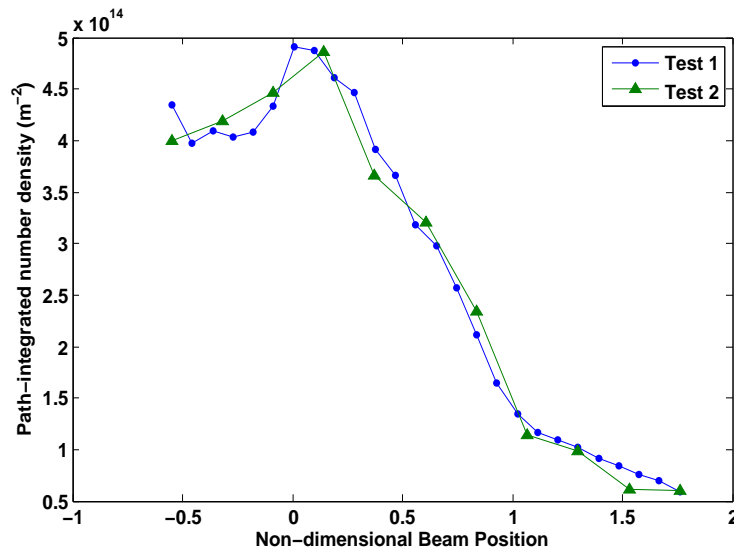


FIGURE 3.9. The 2 kW, 500 V condition was measured at the beginning and end of testing and showed good repeatability.

The path-integrated values for each of the thruster conditions can then be deconvolved using the onion-peeling method described in Sec. 2.1 to yield boron number densities (that are not path integrated) as a function of thruster radius. The deconvolved data is shown in Fig. 3.10 and Fig. 3.11
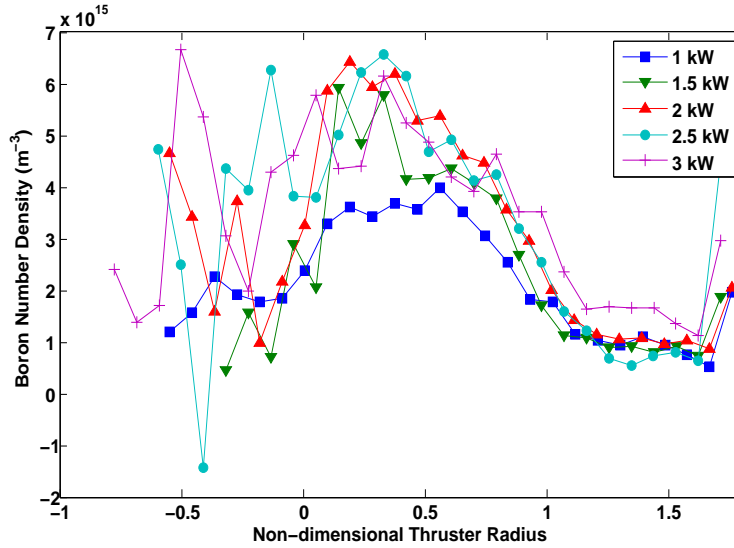
FIGURE 3.10. Boron number densities as a function of channel position. The thruster was held at 500 V for each condition.
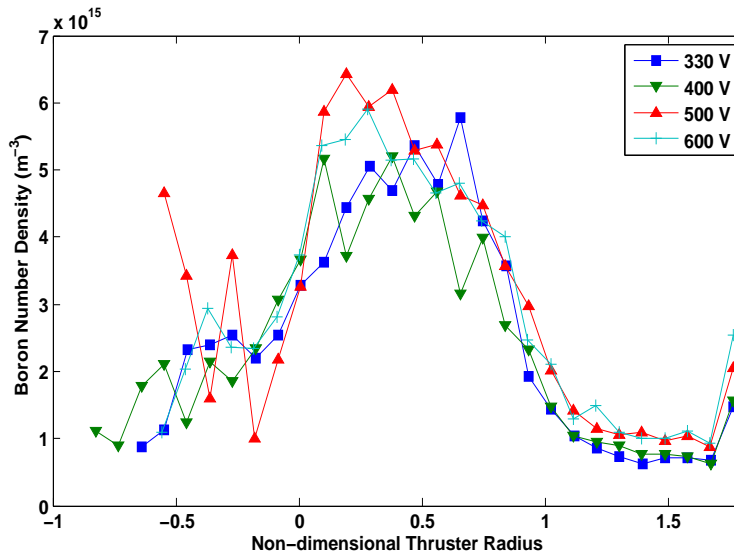


FIGURE 3.11. Boron number densities as a function of channel position. The thruster was held at 2 kW for each condition.

Each path-integrated boron density value was computed from the area under a Gaussian fit. The fit coefficients had associated 95% confidence intervals, which were propagated through the equations in Sec. 2.1 to find uncertainties in path-integrated number densities, as well as through the matrix deconvolution process to find uncertainties in number density.

Figure 3.12 and Fig. 3.13 show the resulting error bars for the 2 kW, 600 V case, which are representative of other cases.
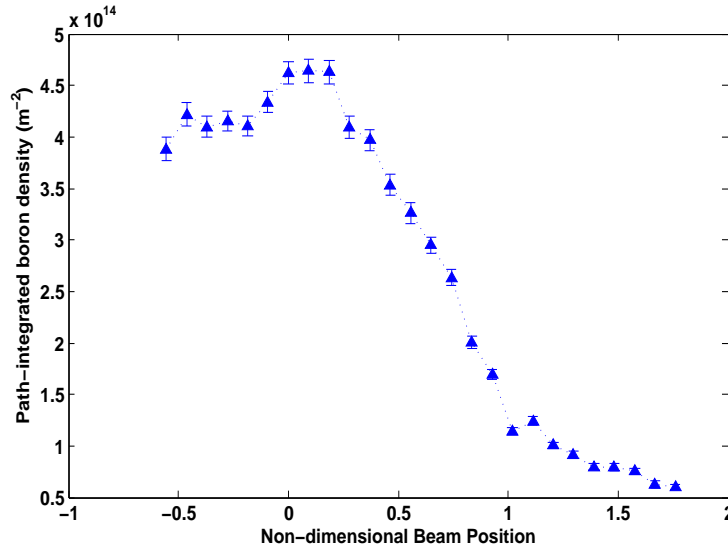


FIGURE 3.12. Path-integrated boron number density for the 2 kW, 600 V thruster setpoint showing representative 95% confidence intervals.
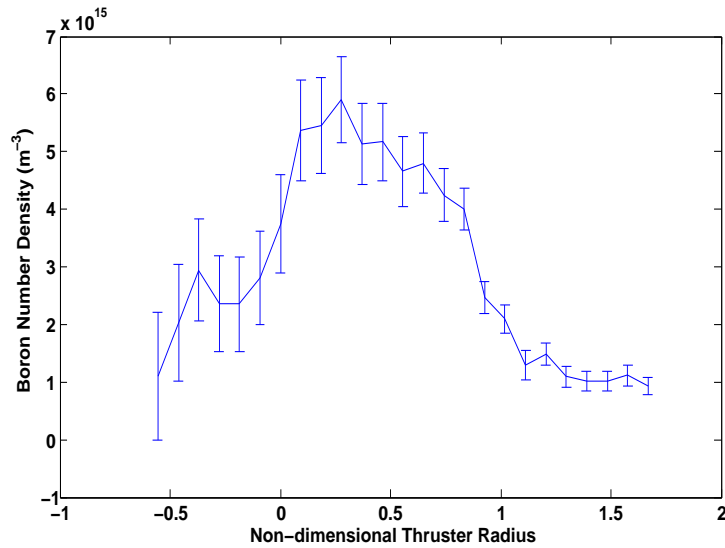


FIGURE 3.13. Deconvolved boron number density for the 2 kW, 600 V thruster setpoint showing representative 95% confidence intervals.

To obtain the boron flux from the thruster, each boron number density needs to be multiplied by the average boron velocity along the thruster axis. These velocities are not

yet well known. However, we can estimate a characteristic velocity from the laser-induced fluorescence (LIF) work done by Tao and Yalin which measured boron speed distributions sputtered from a planar target.[52] The Sigmund-Thompson distribution is a function which describes the velocity distribution of sputtered products.[53] Tao used LIF to measure the flux-based Sigmund-Thompson velocity distribution given by

$$(8) \qquad\qquad f(u) = C \frac{u^3}{(u^2 + v_b^2)^{3-2m}}$$

where $u$ is the boron speed and $v_b$ and $m$ are fit constants found to be 9,500 m/s and 0.17 respectively. The Sigmund-Thompson distribution is only valid for energies of sputtered particles below the energy which would be transferred in a head-on elastic collision, given by

$$(9) \qquad\qquad T_{max} = \frac{4M_1 M_2}{(M_1 M_2)^2} E_{ion}$$

where $M_{1,2}$ are the energies of the incident and sputtered particles, and $E_{ion}$ is the energy of the incident particle. In a Hall thruster environment, incident ion energies can vary between 0 and several hundred eV. Using 0 and $T_{m}ax$ as the limits of integration, along with the measured values of $v_b$ and $m$, a characteristic boron velocity can be found from the first moment of the Sigmund-Thompson distribution, which yields 23 km/s. However, this value is very sensitive to the exact values of $v_b$ and $m$, as well as the limits of integration used. Additionally, Tao only probed the velocity component normal to the planar BN target, which may not be representative of the more complicated thruster geometry. The Doppler broadening observed in the HiVHAc boron spectra gives the velocity profile parallel to the

38

TABLE 3.1. HiVHAc Volumetric erosion rates for each thruster condition.

| Power (kW) | Voltage (V) | Erosion Rate $\left(\frac{m^3}{s}\right)$ | % Statistical Uncertainty |
|---|---|---|---|
| 1 | 500 | $5.08 \times 10^{-12}$ | 5.0 |
| 1.5 | 500 | $5.48 \times 10^{-12}$ | 5.5 |
| 2 | 330 | $6.24 \times 10^{-12}$ | 6.0 |
| 2 | 400 | $6.01 \times 10^{-12}$ | 7.0 |
| 2 | 500 | $7.27 \times 10^{-12}$ | 5.0 |
| 2 | 600 | $7.01 \times 10^{-12}$ | 3.6 |
| 2.5 | 500 | $7.21 \times 10^{-12}$ | 12 |
| 3 | 500 | $8.23 \times 10^{-12}$ | 9.0 |

optical axis. While the velocity component perpendicular to the optic axis is needed, the parallel component gives some insight into a typical boron speed. The spectra have a typical Doppler broadened width of $\sim 0.8$ cm$^{-1}$, which corresponds to a thermal velocity of $\sim 6$ km/s. Due to the lack of more information about the boron speed profiles, a constant 10 km/s was assumed for the average axial boron speed.

Using the number densities found by the CRDS sensor, and the boron speed described above, volumetric channel erosion rates were calculated at each thruster operating condition and are summarized in Table 3.1. The results are also summarized in Fig. 3.14 and Fig. 3.15. As discussed above, the reported uncertainties are from statistical noise only and do not include systematic errors.

As mentioned in Section 2.2, the CRDS sensor probes ground state neutral boron. Any fraction of the boron population which was ionized or electronically excited was not counted. Uncertainty remains in the exact fraction of boron population which resides in the neutral ground state. Estimates of the fraction of boron population which was ionized have been made. Electron-impact ionization cross sections were calculated using methods from Gryzinski.[54] The ionization cross sections are functions of incident particle energy (i.e.
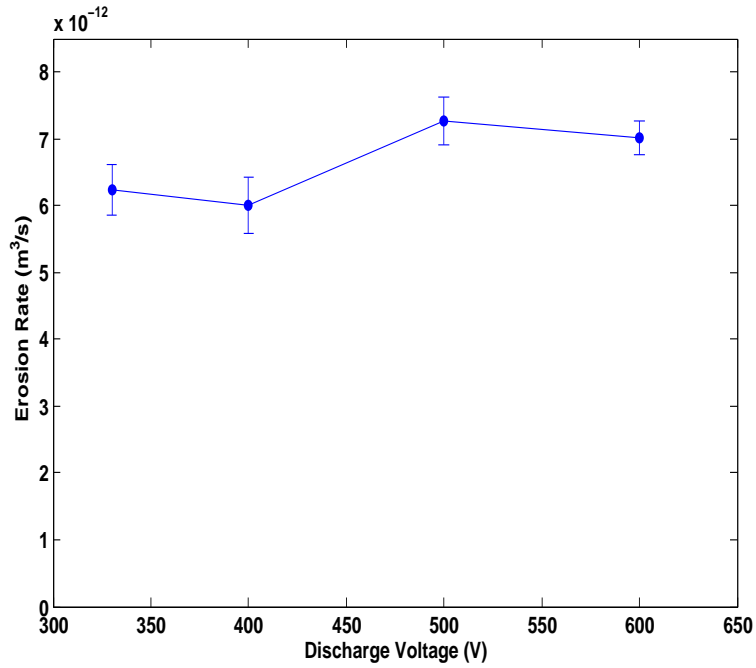
FIGURE 3.14. Channel volumetric erosion rates for varying discharge voltage with a constant 2 kW power.
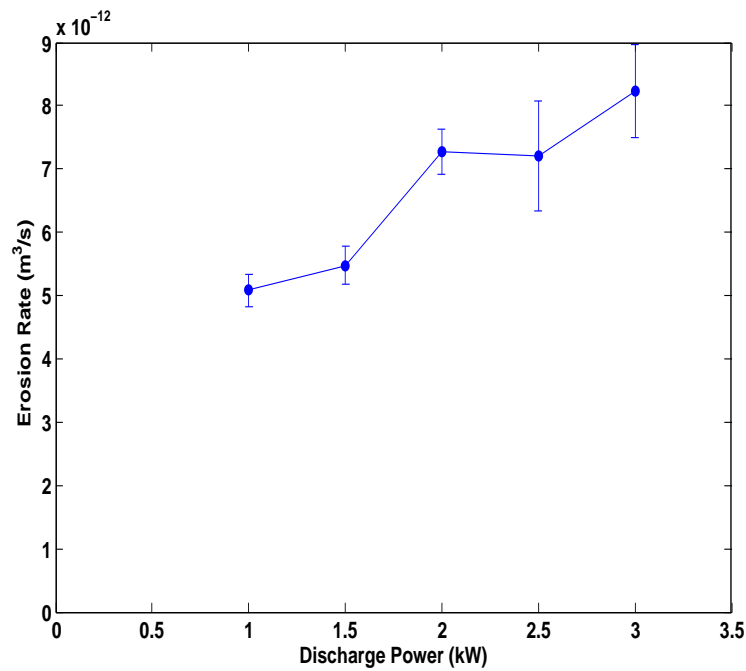


FIGURE 3.15. Channel volumetric erosion rates for varying discharge power with a constant 500 V discharge voltage.

electron speed). An ionization rate constant, $K$, was found by averaging the product of the ionization cross section and the incident electron speed over the Maxwell speed distribution,

$$(10) \qquad K = < \sigma(v)v >_v = \left( \frac{m}{2\pi k_B T_e} \right)^{3/2} \int_0^\infty \sigma(v)v \exp\left( -\frac{mv^2}{2k_B T_e} \right) 4\pi v^2 dv$$

and was used to compute the ionization mean free path

$$(11) \qquad MFP = \frac{V_B}{n_e K}$$

where $v$ is the speed of the incident electron, $k_B$ is Boltzmann's constant, $T_e$ is the electron temperature, $\sigma$ is the ionization cross section, and $n_e$ is the electron density. For example, for $T_e$=10 eV, and $n_e = 10^{12}$ cm$^{-3}$, the mean free path was found to be 54 cm. Table 3.2 gives ionization population fractions for estimated electron temperatures and densities, assuming the boron atoms have to travel ~3 cm before reaching the interrogating laser. No internal diagnostics have been performed on HiVHAc, so a range of likely values were considered. Modeling shows these values can vary over the range considered in Table 3.2 depending on the exact channel location being considered.[55] As can be seen in Table 3.2, the estimated error caused by ionized boron could be fairly small, or quite significant. Additionally, any neutral boron which was not in the ground state was not be counted. However, excited boron population fractions are not known, and estimates have not yet been made. There is a 3% uncertainty in the fundamental boron transition line coefficients used to compute the path-integrated boron number density.[56]

TABLE 3.2. Estimated percent ionized boron after traveling 3 cm.

| | $n_e (cm^{-3})$ | | |
|---|---|---|---|
| $T_e (eV)$ | $10^{11}$ | $10^{12}$ | $10^{13}$ |
| 10 | 0.6 | 5.4 | 43 |
| 20 | 1.2 | 11 | 68 |
| 30 | 1.5 | 14 | 78 |

Note that denser and more energetic plasmas will ionize and excite sputtered boron atoms over shorter distances, thus causing a lower fraction of the boron population to be measured by the CRDS sensor. As the thruster power is increased, a lower fraction of the boron may be counted, skewing the observed erosion rate versus discharge power.

The measured trends in erosion rate are difficult to interpret. Of course, systematic errors exist in the measurement technique itself, including the ionization of boron. Additional potential systematic errors will be discussed in Section 4.3. Provided the observed trends are physical, two things stand out. First, at constant power, the erosion did not change significantly with voltage, suggesting the erosion rate is proportional to the thruster power given by $I_d V_d$, where $I_d$ and $V_d$ are the discharge current and voltage respectively. Second, while the erosion rate increased roughly linearly with discharge power at constant voltage, the trend does not pass through the origin. The origin of this observed behavior is not yet known.

In erosion studies of the H6 thruster by Huang et al., the erosion rate was seen to scale as $I_d V_d^2$.[37] In the H6 thruster, the acceleration zone was observed to move upstream as the discharge voltage increased. Recall that the acceleration zone is the region in which the ions gain the majority of their energy. As the acceleration region grows, it significantly increases the amount of channel exposed to ions which contained enough energy to cause

sputter erosion. Additionally, as the discharge voltage increased, the plasma potential increased, and the energy with which ions impacted the channels walls increased. Above the threshold energy, the sputter yield of many materials (i.e. the number of atoms ejected from a surface per incident particle) increases roughly linearly with incident particle energy.[15] The combination of the increased erosion zone length and the increased sputter yield with discharge voltage account for the erosion rate scaling as $V_d^2$. As the propellant mass flow rate, $I_d$, increases, the plasma density within the channel will increase, thereby increasing the ion flux to the channel walls, causing the erosion rate to scale linearly with $I_d$.

The likely difference in the erosion trends between the H6 and HiVHAc thrusters is that the location of the acceleration zone of the HiVHAc thruster may not change with discharge voltage, unlike other thrusters. Modeling suggests the acceleration zone maintains the same approximate location as the anode voltage is changed.[55] With the acceleration zone remaining constant, the channel wall area which is exposed to energetic ions also remains constant.

Williams et al. used optical emission spectroscopy to study the erosion rate trends of the NASA HiVHAc, 300M, and 457M thrusters.[25] Similar to Huang et al., the erosion rate of the larger 300M and 457M thruster was found to scale as $I_d V_d^2$. However, the HiVHAc thruster erosion was found to be proportional to $I_d V_d$, as was found by the BN CRDS sensor in this work.

CHAPTER 4

# SPT-70 Thruster Erosion Measurements

Stationary plasma thrusters (SPT) are a type of Hall thruster which were developed in the Soviet Union and are largely considered to be the work of A. I. Morozov.[57] Since that time, a variety of SPT Hall thrusters have been developed, the SPT-50 being the first, named for its 50 mm outer channel diameter. In 1971, the satellite Meteor-18 flew an SPT-50 thruster and was the first successful demonstration of a Hall thruster in space. The SPT-70 thruster followed the SPT-50 and is named for its 70 mm channel diameter. Since that time, hundreds of Hall thrusters have been flown without a single failure in space. Despite the age of SPT thrusters, they remain actively researched and continue to improve. In particular, as satellite payloads increase in size, and as missions become longer, there is a need to shift towards higher-power thrusters capable of larger xenon throughput, larger $\Delta V$, and therefore longer lifetimes. Sputter erosion remains a problem for these devices and is one of the most significant life-limiting factors. Additionally, there remains a lack of knowledge regarding the speed and direction of ejected boron atoms. Since the SPT thrusters are commonly used on commercial satellites, there is desire to further characterize the erosion process, as sputtered boron can condense on satellite solar panels and other critical components.

This chapter describes sputtered boron measurements from an SPT-70 thruster using the CRDS sensor. A key difference between the HiVHAc thruster and the SPT-70 is that the SPT-70 is made of a different boron-containing ceramic than HiVHAc. Despite this difference, the CRDS sensor is equally as applicable to the SPT-70. The optical setup used in the SPT-70 erosion measurements was identical to that used in the HiVHAc measurements, including the mirror degradation counter measures. As such, a description of the optical

44

setup will not be repeated here, and the reader is directed to Chapter 3 for details on the CRDS sensor optics. The layout of this chapter is as follows. Section 4.1 describes the SPT-70 testing facilities. Section 4.2 gives the CRDS erosion measurement results, while Sec. 4.3 compares the CRDS results with profilometry measurements.

## 4.1. SPT-70 and Test Facility

The SPT-70 is nominally operated at 660 W discharge power, 300 V anode voltage, 2.23 A discharge current, 27 sccm Xe flow rate, and a specific impulse of $\sim$1440 s. Unlike the HiVHAc thruster, the SPT-70 is designed to only have one operating condition, therefore, erosion trends with set point were not investigated. To demonstrate the sensor's ability to differentiate between small changes in operating condition, the erosion rate was measured at both 300 V and 275 V, despite 275 V not being an intended operating condition. At the beginning of testing, the channel was relatively new with $\sim$10 hours of operation on it.

The vacuum facility housing the thruster was 0.9 m in diameter and 1.2 m in length. The thruster was directed along the axis of the cylinder and the plume was unimpeded for $\sim$15 thruster diameters. The chamber was pumped by three cryogenic pumps: a CT-10, a CT-500, and a custom made cryo sail cooled by a CT-500 compressor for a combined pumping speed on xenon of $\sim$10,000 l/s. The chamber base pressure was $2\times10^{-7}$ Torr and $5 \times 10^{-5}$ Torr with the thruster operating. Due to both the relatively small size of the chamber and its pumping speed, the SPT-70 is approximately the largest thruster which can be operated in the Colorado State University facility. The thruster was mounted on an 18 cm travel motorized translation stage, which translated the thruster vertically. The interrogating laser beam, which was 2 mm downstream of the exit plane, was then swept across the face of the thruster.

A graphite-panel beam dump was placed approximately 15 thruster diameters down-stream of the thruster. The beam dump served to block high-energy xenon atoms ($\sim$300 eV) from impinging on the cryogenic panels, which would have heated them and reduced their pumping capacity. Also, high-energy ions leaving the thruster will impinge upon the vacuum facility surfaces causing sputtered atoms to stream back into the thruster. Graphite has a relatively low sputter yield thereby reducing the number of particles sputtered back into the thruster.

## 4.2. SPT-70 CRDS Erosion Results

Figure 4.1 shows sample CRDS spectra obtained from the SPT-70 operating at the nominal full power condition of 300 V discharge voltage and 2.2 A discharge current. The upper spectrum corresponds to the P=0 position (i.e. with the laser tangent to the inner channel wall), while the lower spectrum corresponds to P=1.5 (just outside the channel). The center of the boron absorption feature is near 0.2 $\text{cm}^{-1}$ (relative frequency). Boron number densities were found using the same methods as in the HiVHAc test. To summarize, a Gaussian was fitted to each absorption spectra and used to compute the area under the absorption curve. Equation 3 was used to find the path-integrated number density, and the 'onion-peeling' technique outlined in Sec. 2.1 deconvolved the path-integrated values yielding absolute boron number densities. Figures 4.2 and 4.3 give path-integrated and deconvolved boron number densities respectively. Each erosion trace (i.e. each trace in Fig. 4.2) required only 15 minutes to obtain.

A total boron flux from the thruster was found using the same methods as in the HiVHAc test. The boron flux from the thruster was found by integrating the product of the boron density and axial boron speed (see Chapter 5) over the thruster exit area. As mentioned
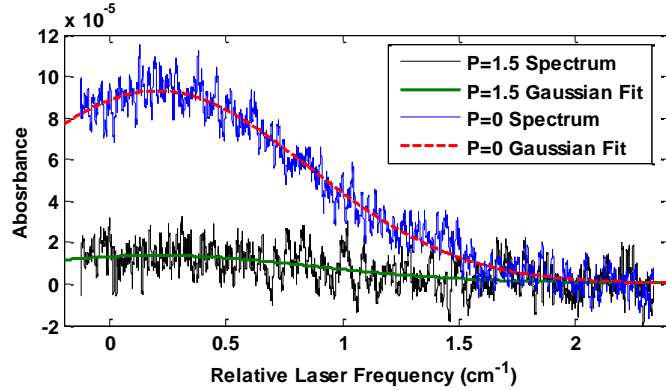
FIGURE 4.1. Sample sputtered boron absorption spectra from the SPT-70 plume operating at 300 V, 2.2 A.
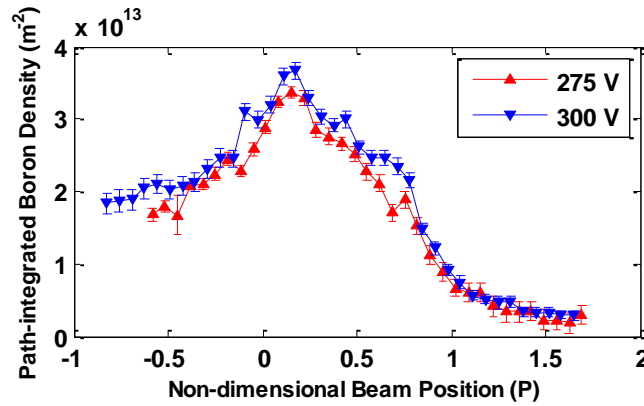


FIGURE 4.2. Path-integrated boron number densities from the SPT-70 running at 2.2 A discharge current and 300 V (blue) and 275 V (red).
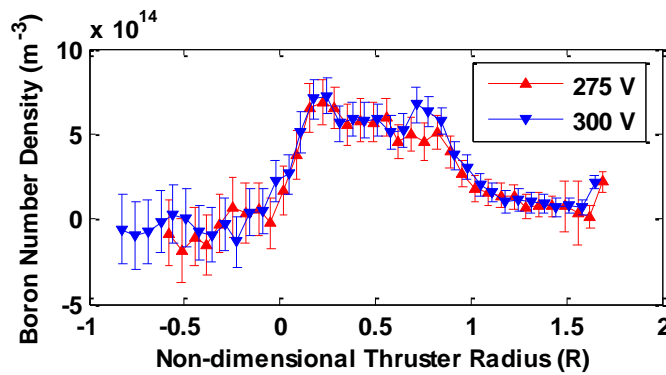


FIGURE 4.3. Boron number densities from the SPT-70 running at 2.2 A discharge current and 300 V (blue) and 275 V (red).

previously, the SPT-70 does not have the same ceramic material as the HiVHAc thruster.

The primary consequence of this difference is the boron velocity distributions are different.

As such, the results from the laser-induced fluorescence (LIF) velocity measurements of boron nitride by Tao et al. may not be applicable to the SPT-70 thruster.[52] Chapter 5 describes LIF measurements of the axial boron speed from the SPT-70 Hall thruster. The key result of those measurements was the first moment of the speed distribution, which was found to be 3840±180 m/s and did not change significantly between the two channel locations measured. Therefore, 3840 m/s was used for each channel location.

TABLE 4.1. SPT-70 volumetric channel erosion rates.

| Discharge Voltage (V) | Erosion Rate $\left(\frac{m^3}{s}\right)$ | % Statistical Uncertainty |
|---|---|---|
| 275 | $2.27 \times 10^{-13}$ | 9.3 |
| 300 | $2.47 \times 10^{-13}$ | 8.1 |

The ratio of the two erosion rates in Table 4.1 is almost exactly the same ratio as their respective discharge voltages (1.088 versus 1.091). While only these two closely spaced voltages were measured, the erosion rate appears to change linearly with discharge voltage, as was found with the HiVHAc thruster.

## 4.3. SPT-70 PROFILOMETRY COMPARISON

As the thruster operates and erodes, the channel walls recede. Mechanical profilometry was used to measure the channel geometry before and after 26.15 hours of operation at 300 V. Figure 4.4 shows a sample profilometer trace before and after thruster operation. Traces were taken at four different locations: two on the inner channel wall and two on the outer channel wall. The eroded volume was found by integrating the difference between the two curves. The total eroded volume was found to be $1.15 \times 10^{-7}$ m³. The uncertainty in each coordinate from the profilometer (Taylor Hobson PGI) was 8 nm. Since the edge of the channel receded ∼100 $\mu m$, the relative error in the profilometer measurement is
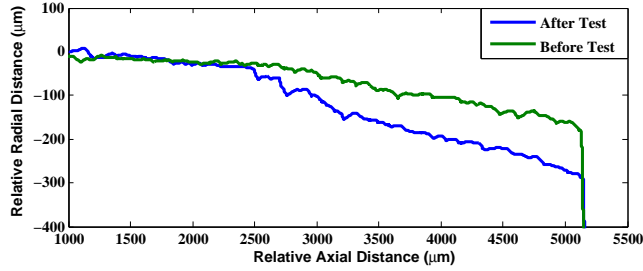
FIGURE 4.4. Profilometry traces of the SPT-70 channel wall before (green, top curve) and after (blue, bottom curve) operating for 26.15 hours at 300 V.

considered negligible in comparison with the uncertainty in the CRDS measurement. The average volumetric channel erosion rate was measured to be $1.22 \times 10^{-12}$ m$^3$/s, which is 5 times larger than was estimated by the CRDS sensor.

The underestimation of the erosion rate by the CRDS sensor was not unexpected, however, a factor of 5 was certainly larger than expected. Huang et al. found CRDS erosion estimates a factor of ~2 lower than profilometry traces of the H6 thruster.[37] Huang largely attributed the systematic error to a poor velocity model. To compute the flux, the authors assumed all boron atoms moved with a speed of 23 km/s (the first moment of the speed distribution measured by Tao et al.) and originated only from the corner of the thruster channel. As explained in Chapter 5, the speed distributions used in the present measurements, although much slower than expected, were directly measured in the SPT-70 plume.

Additionally, Huang estimated the population fraction of boron which was ionized could have been as high as 60%. However, the H6 Hall thruster operates at much higher powers than the SPT-70. Within the SPT-70, electron temperatures are typically only a few eV (<10 eV) and plasma densities are ~$10^{11}$ cm$^{-3}$ near the thruster exit plane.[58] As estimated in Table 3.2, a negligible fraction of the boron population will be ionized by these plasma conditions.

When fast-moving xenon atoms leave the thruster, they will impinge on the inner surfaces of the vacuum chamber. Sputter erosion will occur, and condensable compounds, such as carbon or iron, will stream back into the thruster and condense on the thruster channel walls. These back-sputtered atoms are sputter cleaned off the channel walls, which decreases the rate of channel erosion. Given the chamber housing the SPT-70 is relatively small, the back-sputter rate could be quite high. While this phenomenon will decrease the boron densities measured by the CRDS sensor, it should equally affect the profilometry measurements. Nevertheless, the back-sputter rate was characterized.

A silicon wafer was placed below the thruster, parallel to the exit plane, and slightly behind the exit plane. Back-sputtered atoms which were condensable deposited onto the wafer. A strip of Kapton tape was placed across the wafer such that after thruster operation the tape could be removed, and the deposited film thickness could be measured by profilometry. A silicon wafer was used because it has very low surface roughness making it very amenable to measuring thickness of thin films deposited on its surface. The deposition rate was measured to be only 11 nm/hr. During the 26 hour test, the average channel erosion rate near the channel exit was 3.8 $\mu$m/hr. Therefore, back-sputtered deposition does not seem to explain the discrepancy between the CRDS and profilometry erosion measurements. Additionally, the erosion zone does not appear to have any carbon deposition. The erosion zone is the region within the channel, typically a few mm in length near the exit plane, where the vast majority of sputter erosion occurs. The erosion zone within the SPT-70 still appears white, as opposed to other thruster surfaces which appear black from back-sputtered carbon deposition, which is evidence that this region is being continuously sputter cleaned.

It is well known that the erosion rate of Hall thrusters decreases significantly with time.[59] However, a characteristic time constant for the change in erosion rate is ∼1000 hours of thruster operation. Given the thruster was operated for roughly 28 hours total for both the CRDS measurements and profilometry, the change in channel geometry and channel erosion rate is likely small. The largest change in erosion rate occurs during the beginning of thruster life. The thruster had been operated for less than 100 hours at the time of these measurements. Unfortunately, erosion rate measurements of the SPT thrusters by Absalamov were made at time increments of >100 hours.[60] If the erosion rate changed smoothly during the first few hundred hours, the effect should only be a few percent. Also, profilometry measurements were taken after CRDS measurements. Given that channel erosion decreases with time, this phenomenon could not explain CRDS underestimating the erosion rate.

In order for boron to be measured by the CRDS sensor, it must exit the channel. However, not all boron atoms leave the channel. Some sputtered boron will move back towards the anode and adsorb to the channel and anode surfaces. Recall that the majority of sputter erosion occurs on the portion of the channel near the exit plane. If the differential sputter profile were diffuse, half of all sputtered boron would stream back into the thruster and not be measured by the CRDS sensor. Rubin et al. showed that differential sputter yields are not diffuse for ion impacts away from normal incidence.[15] For an ion angle of incidence of 45°, the majority of sputtered particles will be ejected near 45° on the other side of the normal. The exact angular distribution of the xenon ions impinging on the channel walls is unknown, however, modeling suggests the majority of ions will impact the wall at angle of incidences ∼ 45° or greater.[61] It is unclear exactly what fraction of boron will be sputtered

back into the channel, but it should be clear that there is an upper limit of 50%. The factor of ~2 discrepancy observed by Huang could be explained by boron sputtering back into the channel. Considering there is a factor of ~5 difference between the CRDS and SPT-70 measurements, it can only partially explain the discrepancy here.

To find the eroded volume using profilometry, the un-eroded surfaces were used as reference surfaces, i.e. it was assumed the surface upstream of the erosion zone did not move between the two proflimotery measurements. However, deposition of sputtered particles, from either within the thruster channel or from the vacuum facility walls, could have caused these channel walls to grow during thruster operation, thereby moving the profilometry reference surfaces. Note that the reference surface used and the erosion zone are located only a few mm apart. It is therefore likely that both the reference surfaces and erosion zone had equal amounts of sputtered material deposited on them, and the profilometry measurement was not affected by back sputtering.

As stated in Sec. 2.2, all sputtering from boron nitride is assumed to be as individual boron atoms, as was supported by Rubin et al.[15] However, the more complicated SPT-70 channel material may not follow the same behavior. Boron containing clusters may be sputtered from the SPT-70 channel surface and would not be detected by the CRDS sensor, which currently seems to be the most likely explanation for the observed discrepancy. However, the author was not able to find any data regarding the composition of sputtered products from the SPT-70 channel.

CHAPTER 5

# LASER-INDUCED FLUORESCENCE BORON SPEED

# MEASUREMENTS

The cavity ring-down spectroscopy sensor discussed in the prior chapters measures the boron number density in the plume of an operating Hall thruster. Such measurements provide useful information about the relative change in erosion rate of a Hall thruster. Even more beneficial is the absolute channel erosion rate. As with any particle flux measurement, both the density and velocity are needed. This chapter presents measurements of sputtered boron speed distributions using laser induced fluorescence (LIF) in the SPT-70 thruster plume. To the best of the author's knowledge, the measurements presented here are the first of their kind. Section 5.1 gives a brief overview of relevant past LIF work. Sections 5.2 and 5.3 give the LIF experimental setup and results respectively.

## 5.1. PAST LIF WORK WITH HALL THRUSTERS

The vast majority of laser-induced fluorescence investigations of Hall thrusters have utilized xenon Doppler shifting to map the propellant velocity in the thruster plumes.[62, 63] Such work typically involves probing singly-charged xenon ions near 835 nm and observing their fluorescence near 542 nm. Huang used xenon LIF to map the acceleration region (i.e. the region in which the majority of xenon acceleration occurs within the thruster channel).[64]

LIF measurements of xenon ions have also been used to map xenon speed distributions in the plasma sheath formed at the plasma boundary. Such intra-sheath speed distributions give information about the plasma potential distribution shape in the sheath, and therefore,

give insight into secondary electron emission yields. Williams characterized cathode erosion by observing LIF spectra of molybdenum and tungsten.[65]

As was mentioned in previous chapter, Tao et al. used LIF to measure speed distributions of sputtered boron atoms from a boron nitride target.[52] The planar boron nitride target was sputtered with an argon and xenon ion source (separately). The velocity component perpendicular to the target was found to follow the Signmund-Thompson distribution, which is given by

$$(12) \qquad\qquad\qquad f(u) = \frac{u^3}{(u^2 + v_b^2)^{3-2m}}$$

where $u$ is the boron speed and $v_b$ and $m$ are fit constants found to be 9,500 m/s and 0.17 respectively. Tao showed these coefficients varied only a few percent even when the impinging atom energy and angle were changed over wide ranges and when the impinging gas was changed from argon to xenon. The first moment of the boron speed distribution was found to be 23 km/s, which, prior to the work presented in this chapter, was assumed to be a characteristic boron speed within the plume of a Hall thruster.

The SPT-70, however, uses a different boron containing ceramic than was studied by Tao et al. Additionally, Tao only investigated the velocity component normal to the planar target, which is not representative of the boron axial velocity actually found in a Hall thruster.

## 5.2. SPT-70 Boron LIF Experimental Setup

Boron speed measurements were performed by measuring Doppler shifts of boron atoms within the plume of the SPT-70 Hall thruster. Figure 5.1 shows the geometry of the LIF

setup. The pump laser was directed along the axis of the Hall thruster, which excited the same boron transition near 250 nm as was used in the CRDS sensor. The excited boron decayed back to the ground state, emitting a photon at the same 250 nm transition. The exact wavelength at which boron absorbed was shifted by the Doppler shift. The magnitude of the shift is given by

$$\Delta\nu = \frac{\vec{V} \cdot \hat{k}}{\lambda}$$
(13)

where $\Delta\nu$ is the frequency shift, $\vec{V}$ is the particle's velocity, $\lambda$ is the wavelength, and $\hat{k}$ is the unit vector of the pump beam propagation direction. As can be seen in Fig. 5.1, the vector $\vec{k}$ was along the thruster axis. The measured Doppler shift was therefore only due to the boron velocity component along the thruster axis. The fluoresced light was emitted isotropically. A lens was placed to the side of the thruster and focused fluoresced light into a fiber optic for collection.

The pump laser was scanned over the Doppler-broadened boron absorption line as the fluoresced light was collected. The amount of fluoresced light at a particular wavelength was a measure of the boron population which had a velocity that satisfied

$$\nu = \nu_0 \left( 1 + \frac{\vec{V} \cdot \hat{k}}{c} \right)$$
(14)

where $\nu_o$ is the unshifted absorption frequency, and $c$ is the speed of light. The fluorescence distribution is therefore proportional to the boron axial speed distribution. Note this assumes
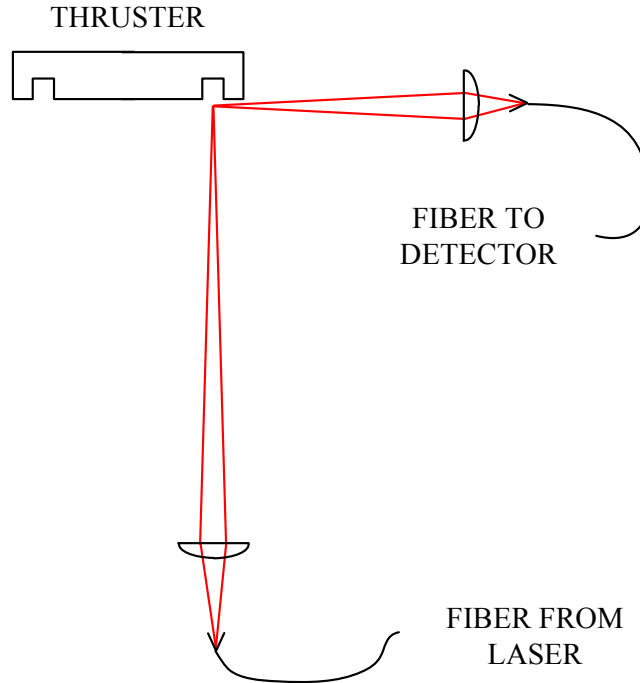
FIGURE 5.1. Geometry of the LIF speed measurement. The pump beam (vertical red beam) was directed along the thruster axis. The waist of the collection volume (depicted as red horizontal beam) was overlapped with the waist of the pump beam.

pressure and natural broadening are negligible compared to Doppler broadening, which is a good assumption in the largely collisionless thruster plume.

Figure 5.2 shows the air-side optical setup for the LIF experiment. The laser used was a frequency-quadrupled external-cavity diode laser (Toptica, TA-FHG110) producing about 18 mW of CW UV light, and was capable of mode-hop free scanning over an extent >75 GHz. An infrared test beam from the laser was sent into a wavemeter (Burleigh, WA-1000) for wavelength measurement. The beam splitter directed about 10% of the primary output power to a photodiode. Each fluorescence measurement was divided by the photodiode signal in order to normalize the effect of changing laser power. An acousto-optic modulator (Neos, 35110-2-244-BR) modulated the beam in a 10 kHz square-wave signal created by a frequency generator (FG). Modulating the pump beam allowed for phase-sensitive detection
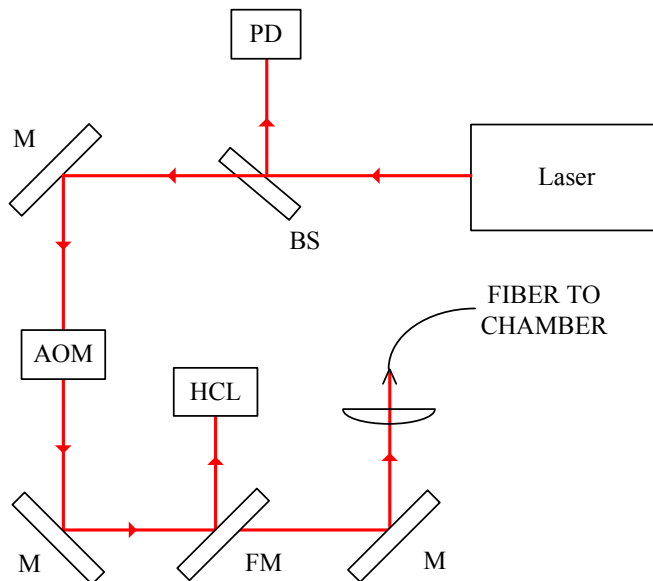
FIGURE 5.2. Schematic of the air-side LIF optical setup. BS:90-10 beam splitter, PD:photodiode, M:steering mirror, AOM:acousto-optic modulator, FM:flip mirror, HCL:hollow-cathode lamp

to be employed using a lock-in amplifier. When the flip mirror (FM) was up, the beam was directed into a hollow cathode lamp, the purpose of which is described below. When the flip mirror was down, the beam was coupled into 500 $\mu$m diameter UV fused silica fiber which was passed into the chamber.

From Eqn. 14, one must know the unshifted absorption frequency, $v_0$, to calculate the boron speed. A hollow cathode lamp (HCL) was used as a zero-frequency reference. The HCL is a sealed glass cylinder which contains a low pressure ($\sim$133 Pa) neon gas. A DC power supply provided 7 mA of current, nominally at 360 V, between the anode and boron-layer cathode creating a plasma. The neon plasma sputter eroded the boron-layer cathode, ejecting boron atoms into the plasma. Both the anode and cathode were cylinders with holes through their centers for the beam to pass through. Due to the cylindrical symmetry of the anode and cathode, the sputtered boron had zero net velocity. As a result, the Doppler-broadened boron absorption spectrum was centered on the unshifted frequency $\nu_0$.
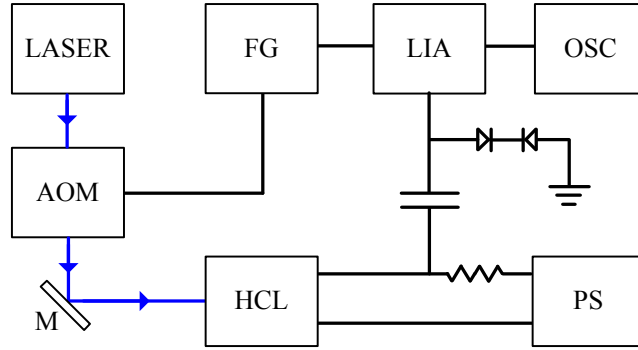
FIGURE 5.3. Diagram of the circuit used to decouple the hollow cathode lamp signal. The laser-beam path is shown in blue and the electric connections in black. AOM:acousto-optic modulator, FG:function generator, LIA:lock-in amplifier, OSC:oscilloscope, PS:DC power supply

When the laser was tuned to resonance with the boron in the HCL, electrons in the boron were excited, decreasing the energy required to ionize them. The excited boron atoms were then more frequently ionized by electron-impact collisions, reducing the voltage needed to sustain the plasma discharge. The change in the plasma conductivity due to the laser is called the optogalvanic effect. Since the beam was modulated by the AOM, the change in voltage also followed the square wave created by the FG. Figure 5.3 shows the circuit used to measure the HCL signal. A 0.47 $\mu$F capacitor coupled only the AC component of the lamp current (measured as the voltage across a 11.6 $k\Omega$ ballast resistor) to a lock-in amplifier, which measured signals at the same frequency as the reference signal created by the FG. Two 5 V Zener diodes between the lock-in amplifier and ground acted as a transient suppressor, grounding any large signals such that they did not damage the lock in. Finally, the HCL signal was measured on an oscilloscope. The amplitude of the HCL signal was quite small and required a lock-in time constant of 30 seconds.

The pump beam in Fig. 5.1 was focused to 1.6 mm diameter using a 125 mm focal-length lens which sat ~76 cm downstream of the thruster. The focal point was placed at the

location $P=0.5$ from the CRDS measurements, which is 2 mm downstream of the thruster exit plane at the channel center. A 2.54 cm diameter, 75 mm focal length lens collected fluoresced light and focused it into a 550 $\mu$m core diameter fiber. The collection volume had a 1.6 mm diameter focus which was centered on the pump beam focus. The interrogated volume was the overlapped region between two perpendicular beams with 1.6 mm diameters.

In order to have a linear response of fluoresced light and pump power, the pump beam intensity must be well below the saturation intensity given by

$$(15) \qquad\qquad\qquad I_{sat} = \frac{h\nu}{\sigma\tau_s}$$

where $h\nu$ is the photon energy, $\sigma$ is the peak absorption cross section, and $\tau_s$ is the excited-state lifetime. The excited-state lifetime is found from the reciprocal of the Einstein $A$ coefficient for the transition, which is $A = 1.67 \times 10^8$ s$^{-1}$. The absorption cross section was computed to be $7.8 \times 10^{-18}$ m$^2$ using equations from Hilborn and the aforementioned Einstein coefficient.[66] Quenching was ignored, as the environment downstream of a Hall thruster is largely collisionless. For the boron transition in question and using a 1.6 mm diameter beam, $I_{sat}$ is 1.7 kW/cm$^2$ assuming zero quenching. The pump beam power was $\sim$5 mW, giving an intensity at the focus of 0.25 W/cm$^2$, far below the saturation intensity.

Once collected in the fiber, the fluoresced light was passed through a dispersive grating monochromator centered on 250 nm and detected by a photomultiplier tube (PMT). The monochromator used a 1200 grooves/mm UV holographic grating (Thorlabs, GH25-12U), allowing a $\sim$5 nm wide band of wavelengths to pass at $\sim$65% efficiency. The PMT signal was measured by a lock-in amplifier.
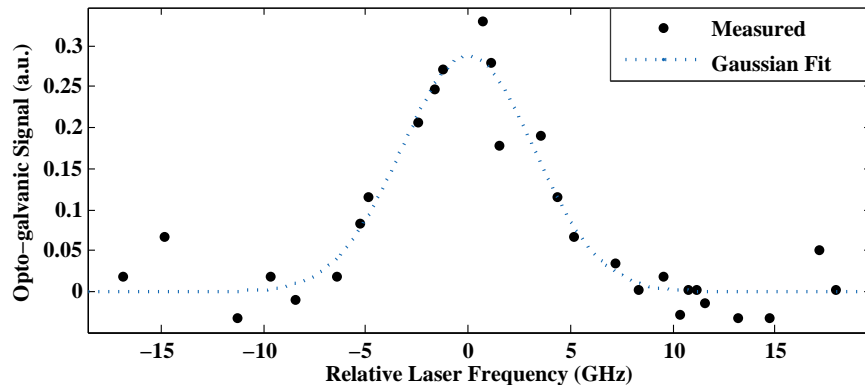
FIGURE 5.4. Measured boron absorption spectrum from the hollow cathode lamp.

## 5.3. SPT-70 LIF RESULTS

Figure 5.4 shows the optogalvanic signal from the hollow cathode lamp as the laser was scanned over the boron absorption line. Given the low pressure and high temperature in the lamp, the spectrum is almost completely Doppler broadened. The width corresponds to a boron thermal temperature of 815 K. The center of this distribution is the unshifted boron absorption frequency $\nu_0$, which was found to within $\pm 0.1$ GHz.

Once the unshifted boron frequency was found, the LIF spectrum from the SPT-70 plume was measured. Figure 5.5 shows the LIF spectrum of boron in the thruster plume. The channel location was $P=0.5$ (the center of the channel), and the thruster was operating at 300 V and 2.2 A. A positive frequency shift means the boron was moving towards the pump laser (away from the thruster).

Figure 5.6 shows the LIF spectra of boron at channel locations $P=0.5$ (channel center) and $P=0.25$ (half way between the channel center and wall). The frequency axis was converted to boron speed using Eqn. 13. Surprisingly, they are almost exactly the same. Additional insight can be gained from looking at the Doppler broadened spectra obtained via CRDS, which gives the speed along the CRDS optical axis (perpendicular to the velocity
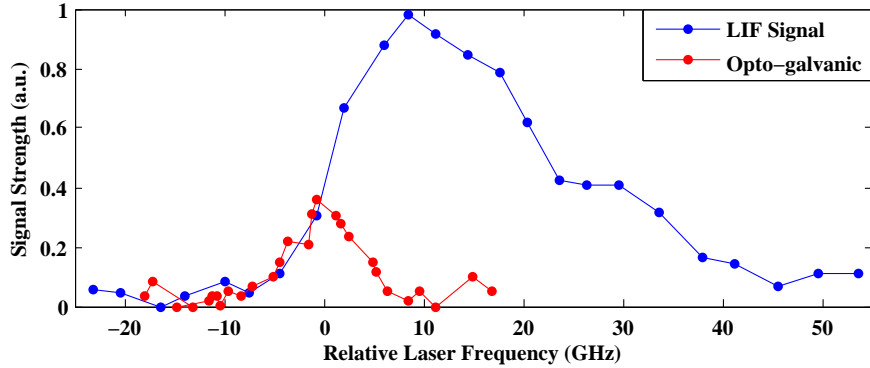
FIGURE 5.5. Measured boron LIF spectrum (blue) in the SPT-70 plume at channel location $P=0.5$ (center of channel) at 300 V 2.2 A. The HCL spectrum (red) provided a zero-frequency reference.

component measured by LIF). The CRDS spectra are more difficult to interpret, as they contain contributions from boron along the entire beam path. Nevertheless, the width of the Gaussian fit to the spectra was nearly constant as the laser was scanned across the channel, which is consistent with the similar LIF velocity distributions. The half width at half max of the Gaussian corresponds to a boron speed of 4920±200 m/s, which is also similar to the observed boron axial speeds.

Additionally, a small fraction of the boron population was observed to move back into the thruster channel (i.e. speed<0). There could be two possible explanations for this. Boron which had be previously sputtered from the SPT-70 channel condenses on various surfaces of the vacuum chamber, which will in turn be back sputtered into the channel, giving a negative Doppler shift. However, the area of the interior surfaces of the vacuum chamber is orders of magnitudes larger than that of the channel, and therefore, orders of magnitude less boron should be sputtered back into the thruster. A more likely explanation for boron moving backwards into the thruster is collisions with xenon atoms. Assuming hard-sphere collisions between xenon and boron, the boron mean free path is ∼95 mm near the channel
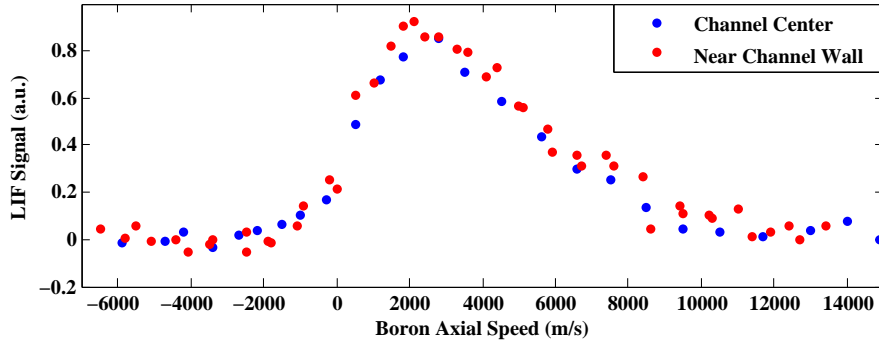
FIGURE 5.6. Comparison of boron spectra measured in the SPT-70 plume at channel locations $P=0.5$ (channel center, blue) and $P=0.25$ (near channel wall, red).

exit, which is sufficiently short to have a small fraction of boron change direction prior to exiting the plume.

The measured boron velocity profile, shown in Fig. 5.6, does not follow a Sigmund-Thompson distribution closely enough to produce a reasonable fit. The primary qualitative difference between the measured profiles and the Sigmund-Thompson distribution is that the measured profiles do not have the long tail characteristic of the Sigmund-Thompson (i.e. that the Sigmund distribution drops to 0 much more slowly than the measured profile). The first moment of the distribution is particularly informative as it is needed to compute boron flux from the channel. The first moment was found to be 3840±180 m/s, which was used in the previous chapter to compute boron flux from the SPT-70.

# HIGH-FINESSE UV OPTICAL CAVITY WITH $CaF_2$ PRISM RETROREFLECTORS

This thesis has largely focused on the use of cavity ring-down spectroscopy (CRDS) as a means to measure sputtered boron in the plume of a Hall thruster. As a corollary project to the boron CRDS sensor, work was done to improve the finesse and bandwidth of optical cavities in the UV region through the use of calcium fluoride prism retroreflectors. This chapter discusses the design, fabrication and testing of such prisms as well as their implications for electric propulsion diagnostics.

In almost all cavity-enhanced work, dielectric mirrors have been used to create the cavities because of the ability to obtain super mirrors with losses less than ∼100 parts per million. However, the layer thickness in dielectric mirror coatings is specifically selected for a design wavelength, as such, spectral coverage of the highest reflectivity mirrors is limited to only a few percent of a central design wavelength. Broadband measurements, such as those needed for simultaneous species detection with a single cavity, are therefore limited. Also, as one moves to the ultraviolet (UV) spectral region, the loss in even the best dielectric mirrors increases substantially. In the visible and near-infrared (NIR) regions, mirror reflectivities can exceed 99.999%. However, the best reflectivity at 250 nm quoted by many suppliers was ∼99.8%. Achieving high reflectivity in the UV region is difficult due to increased absorption and scatter loss in the coating materials.

High-finesse optical cavities have been constructed using Brewster-angle prism retrore-flectors for use in the visible and infrared regions[67, 68]. Prism retroreflectors utilize two

45° total internal reflections (TIR), which can, in principle, provide high reflectivity over all wavelengths as long as the prism material loss is sufficiently low, the surface scatter loss is low, and the critical angle condition can be met. Lehmann et al. describe the operation of the prism ring cavity in great detail[68]. Prisms constructed of fused silica demonstrated optical loss below 400 ppm over wavelengths spanning ∼550 to 1064 nm simultaneously using a supercontinuum light source[69]. The company Tiger Optics has developed a wavelength-multiplexed fused silica prism-cavity sensor for simultaneous multiple species detection[70]. The Tiger Optics' fused silica prisms have demonstrated reflectivities as high as 99.9987% in the telecom NIR region[71]. The loss of fused silica rises further in the IR region, and is limited to wavelengths of ∼<1.8 $\mu$m. Barium fluoride is a promising mid-IR material that should allow high performance prism retroreflectors for wavelengths up to ∼5.2 $\mu$m.

As one moves farther into the UV spectral range, bulk scattering loss can prohibit achieving high-reflectivity prisms, as it scales as $1/\lambda^4$. Calcium Fluoride ($CaF_2$) is a widely used material for deep-UV applications due to scatter loss that is approximately two orders of magnitude lower than fused silica and good transmission deep into the UV[72]. In this chapter, we present a high-finesse and broadband optical cavity in the UV region using Brewster-angle prisms constructed from $CaF_2$. The prisms follow the same design as in Lehmann et al.[68] Prior to construction of the $CaF_2$ prisms, the transmission of superpolished $CaF_2$ windows were measured as a feasibility assessment of $CaF_2$ prisms. Continuous-wave CRDS at 250 nm was used to measure the spatially-resolved transmission of the $CaF_2$ windows. The optical loss was correlated with spatially-varying stress-induced birefringence. Final prism reflectivity was measured using continuous-wave CRDS at 250 and 500 nm. Prism

surface roughness and quality were measured using white-light interferometry. Limitations to the $CaF_2$ prisms are also discussed.

The layout of the remainder of this chapter is as follows. Section 6.1 gives details on the prism retroreflector cavity operation. Section 6.2.1 gives the experimental setup for measuring $CaF_2$ window optical loss. Section 6.2.2 discusses the optical-loss measurement results. Section 6.3.1 gives the specifications of the $CaF_2$ prisms, and Section 6.3.2 gives the experimental setup and results for testing of the prism cavity. Conclusions and implications for electric propulsion diagnostics are given in Section 6.4.

## 6.1. Prism Retroreflector Cavity Design and Operation

Figure 6.1 shows a schematic of the ring cavity formed by two prism retroreflectors[68]. The beam circulates around the cavity, going through points, $R_{1,2...8}$. Total internal reflection occurs at points $R_{2,3,6,7}$. The beam enters and exits each prism at Brewster angle at points $R_{1,4,5,8}$, requiring p-polarized light for low loss. If both prisms were perfectly aligned to Brewster angle, no light would be coupled into, or out of, the cavity. As such, the first prism is intentionally deviated from Brewster angle, typically by $\sim 1°$. Once deviated from Brewster angle, there will be a finite reflection at $R_4$ where the beam enters the cavity, and at $R_1$, where the beam exits the cavity for detection. However, the reflection coefficient at $R_4$ will be small, and the majority of light will transmit through the surface and exit through face $\overline{CD}$. Measurements are performed by exciting the cavity with $P$-polarized light and detecting the amount of light coupled out of the cavity at $R_1$. The operation of a prism cavity is described in great detail by Lehmann et al.[68]

The open-air path length between the prisms allows for an analyte, often gaseous, to be interrogated as in any other cavity-enhanced technique. Additionally, an evanescent wave
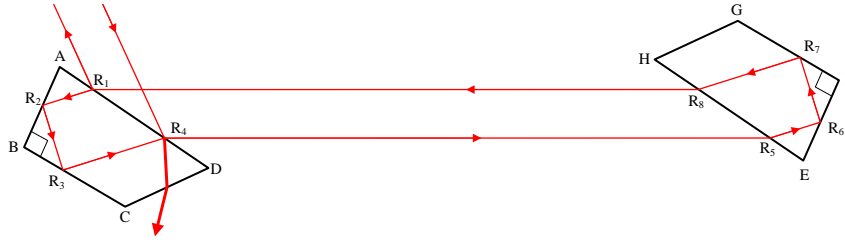
FIGURE 6.1. Ray-tracing schematic of prism retroreflector cavity.

will be created at the TIR surfaces. Provided the critical angle condition could still be met, evanescence wave spectroscopy could be performed on these surfaces[73].

In order to satisfy the critical angle condition for TIR, the material index must be higher than $\sqrt{2}$, which limits the use of $CaF_2$ to wavelengths below 3.3 $\mu$m. In practice, however, small angular errors in the prism construction, and the need to deviate the first prism from Brewster angle, limit the use to below wavelengths of $\sim$1 $\mu$m. $CaF_2$ is often quoted as being optically transparent at wavelengths as low as $\sim$150 nm. However, for use in prism retroreflectors, bulk loss becomes too high for wavelengths shorter than $\sim$220 nm[72].

Additionally, birefringence in the prism material will cause $p$-polarized light to be converted to $s$-polarized light and quickly lost at the Brewster surface. Despite its high symmetry, Burnett showed calcium fluoride exhibits anisotropic intrinsic birefringence[74]. However, for light propagation along <111> (i.e. the beam wave vector $\vec{k}$ normal to the Miller plane (111)), the intrinsic birefringence is 0. In total, there are 7 directions of propagation for which there is no intrinsic birefringence: three in the <100> directions and four in the <111> directions. Stress-induced birefringence also exists due to residual stresses remaining from crystal growth. Burnett also measured the stress-optic tensor, which relates mechanical crystal stress to birefringence[75]. The measured tensor shows the amount of stress-induced birefringence to be near 0 for light propagating along the <111> crystal axis at 632 nm and

still relatively small at 250 nm. Therefore, the optical axis is aligned to the <111> crystal axis in both the CaF$_2$ test windows and in the prism retroreflectors. Note that the <111> axes are not orthogonal. Since the three beams within the prism are orthogonal to each other, they cannot all be aligned to <111> crystal axes. Figure 6.2 shows the orientation of the crystal axes within the prism. Minimum loss due to stress-birefringence should occur when the two parallel beams are aligned with the <111> axis, and the third beam 19° off of a <111> axis. It is difficult to predict the contribution of stress-birefringence to the total optical loss, as the internal crystal stress varies throughout the crystal. However, even a low average birefringence of $\sim 0.4$ nm/cm can result in 1000 ppm loss per prism.
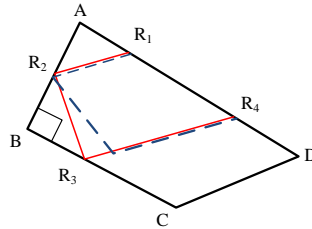


FIGURE 6.2. Top view of prism retroreflector showing orientation of the <111> crystal axes (dashed blue) to the optical axis (solid red). Note that all vectors shown are in the plane of the image.

Light will be lost to scatter at the Brewster surface $\overline{AD}$ and at the two TIR surfaces. Equations for surface scatter loss, given in Lehmann et al.[68], show that the loss scales as $1/\lambda^2$. For UV applications, it is therefore necessary to obtain very low roughness surfaces. An RMS surface roughness of 1 Å will result in $\sim$50 ppm loss per prism.

## 6.2. CaF$_2$ Sample Testing

Given the high cost of prism construction, total optical loss of two superpolished high purity CaF$_2$ windows obtained from different vendors were measured to assess the feasibility

of achieving high $CaF_2$ prism reflectivity. The windows were 10 mm thick and 25 mm in diameter. They were cut from a single $CaF_2$ crystal which was grown along the <111> axis. The <111> axis was oriented at internal Brewster angle (34.3° at 250 nm) relative to the circular input/output surface normal. The two circular surfaces were superpolished to < 1Å surface roughness, which was confirmed both by the polisher and independently using white light interferometry. The absolute stress birefringence was specified by the manufacturer as <0.5 nm/cm at 633 nm. The total optical loss of the windows was measured using cw-CRDS, the experimental setup for which is discussed in Sec. 6.2.1. Optical loss measurement results are discussed in Sec. 6.2.2.

6.2.1. OPTICAL LOSS EXPERIMENTAL SETUP. Cavity ring-down spectroscopy (CRDS) is an ultra sensitive laser measurement technique which uses the enhanced path length of a high-finesse cavity to measure very small optical losses. In CRDS, a high-finesse cavity is excited with a laser, in this case a continuous-wave laser. The cavity is formed by two high reflectivity dielectric mirrors. An acousto-optic modulator (AOM) is used to extinguish the laser beam once significant power is built up between the cavity mirrors. The remaining light within the cavity will leak out through the small transmission of high reflectivity (HR) mirror, yielding an exponential decay with time. The $1/e$ point of the decay is termed the ring-down time, which can be used to calculate the total loss within the cavity (including loss of the mirrors themselves). The wavelength of interrogation was 250 nm generated by a frequency-quadrupled external-cavity diode laser (Toptica, TA-FHG110).

The $CaF_2$ window was placed within the cavity at Brewster angle allowing $p$-polarized light to enter and exit the window with low loss. Also, as mentioned previously, the <111> crystal axis is at Brewster angle relative to the window surface normal and can therefore be

aligned to the optical axis. In order to decouple the loss contribution of the CaF$_2$ window and that from the cavity mirrors themselves, the ring-down time was measured with and without the window in place. The resulting difference is the loss from only the window. Figure 6.3 shows the loss measurement setup with the window inside the cavity. To also allow measurements without the windows, the back HR mirror was placed on a translation stage such that it could be moved transverse to the optical axis to compensate for the 4.4 mm lateral shift when the beam passed through the window at Brewster angle. Two translation stages moved the window in the plane of its circular face, allowing optical loss to be measured at different points on the window.



FIGURE 6.3. Schematic of CRDS optical-loss measurement apparatus. AOM: acousto-optic modulator, MM: mode-match telescope, M: steering mirror, P: linear polarizer, HR: high reflectivity mirror, PMT: photomultiplier tube, CaF$_2$: test window.

As mentioned earlier, birefringence in the CaF$_2$ crystal will convert $p$-polarized light to $s$-polarized light, which has a much higher Fresnel reflection coefficient at the Brewster surface. Since the polarizer (100,000:1 extinction ratio) prior to the optical cavity only transmits $p$-polarized light, any light reflecting off the window Brewster surface is a direct consequence of polarization rotation caused by crystal birefringence. The ratio of the amplitudes of the ring-down signals measured on PMT 1 to PMT 2 is a measure of the relative amount of crystal birefringence integrated along the optical beam path at that location. As the window was

translated, the aforementioned ratio was found to change significantly. The spatial variation in crystal birefringence was also measured using crossed polarizers, as depicted in Fig. 6.4, and showed near perfect correlation with the CRDS birefringence measurement. Note that the AOM and mode-match telescope are not necessary for the crossed-polarizer measurement, but were left in place to ensure the beam interrogated the same point on the window.
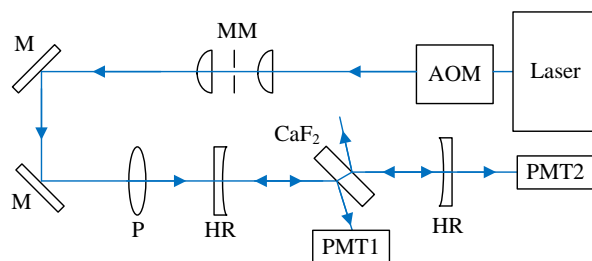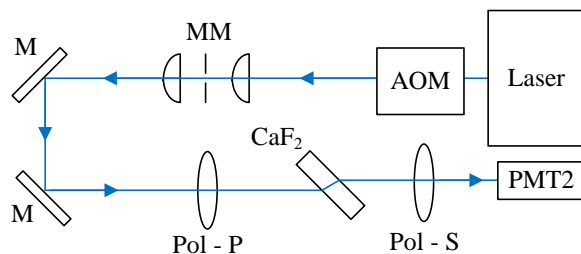


FIGURE 6.4. Schematic of crossed polarizer measurement apparatus. AOM: acousto-optic modulator, MM: mode-match telescope, M: steering mirror, P: linear polarizer, HR: high reflectivity mirror, PMT: photomultiplier tube, Pol-P: $P$-oriented polarizer, Pol-S: $S$-oriented polarizer.

6.2.2. OPTICAL LOSS MEASUREMENTS RESULTS AND DISCUSSION. Figure 6.5 shows the total optical loss and relative birefringence of the $CaF_2$ window which exhibited the lowest loss at 250 nm. The same $CaF_2$ supplier was used for the $CaF_2$ window discussed here and the prisms. The window supplied by the other manufacturer showed loss approximately 3 times higher and is not discussed in this section. Optical loss was measured over a ~1 cm region with a 0.64 mm measurement spacing. The beam size at the window was 0.4 mm. The minimum, maximum and mean window loss were observed to be 340±60, 2420±60, and 1130±60 ppm respectively. The relative birefringence showed very high spatial correlation with the total loss, though not perfect correlation. Such correlation suggests that stress birefringence is a large contributor to the overall optical loss. However, other mechanisms such as crystal impurities may also contribute and explain the imperfect correlation. As discussed

in Sec. 6.1, CaF$_2$ does possess intrinsic birefringence, however not along the $< 111 >$ axis to which the beam is aligned[74]. Additionally, the relative orientation between the interrogating laser and the crystal axes did not change throughout the test. Therefore, the spatially varying contributions of the birefringence must be from stress-induced birefringence, which can vary throughout the crystal.
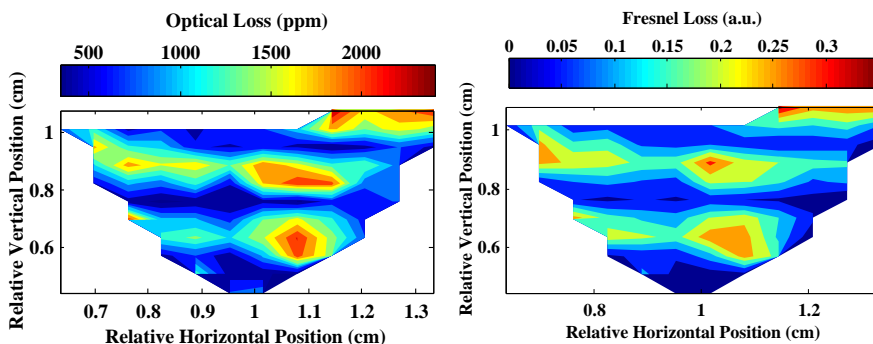


FIGURE 6.5. Optical loss from CRDS (left) and the birefringence measured from crossed polarizers (right) at 250 nm.

Note that the beam path length through the window is 12.1 mm (not multiplied by $n$), while the path length through our prisms is 29.7 mm. Also, the beam must transmit through two Brewster surfaces in the window, but no TIR surfaces, while each prism has two Brewster surfaces and two TIR surfaces. In order to scale the loss of the window to an estimated prism loss, the window loss is multiplied by the ratio of beam path length in the prism to that of the window or 2.45. Not only does this factor include the extra path length within the prism, but it also approximately accounts for the two additional surface interactions the loss of which is additive with bulk loss. Scatter loss at a TIR surface contributes $\sim$5 times as much scatter loss than at a Brewster surface for the same roughness, so the scaling factor may somewhat underestimate the total surface scatter loss but should still provide a close estimate.

Using the scaling mentioned above, the window losses translate to a minimum, maximum and mean estimated prism reflectivity of 99.92%, 99.41%, and 99.72% respectively. Such reflectivities were deemed sufficiently high to warrant constructing $CaF_2$ prisms. The best available dielectric mirrors have reflectivites approaching 99.8%. Based on the loss estimates presented here, $CaF_2$ prisms have the potential to exceed the performance of dielectric mirrors for single-wavelength operation, as well as provide UV-broadband operation.

## 6.3. $CaF_2$ PRISM CAVITY

A pair of Brewster angle $CaF_2$ prism retroreflectors have been constructed and tested. This section discusses their specifications and performance. Section 6.3.1 gives the prism geometry and specifications. Section 6.3.2 gives the experimental setup for the prism testing and their measured performance.

6.3.1. $CaF_2$ PRISM SPECIFICATIONS. Figure 6.6 shows a top-view drawing of the prism with relevant dimensions to which the prisms were manufactured. The prism height (i.e. the dimension out of the page) is 12.5±0.2 mm. The first prism has all planar surfaces, while surface $\overline{EF}$ (see Fig. 6.1) on the second prism is spherical with a radius of curvature of 6.7±0.1 m with the tangent point centered on the square face. The spherical surface focuses the beam, creating a stable cavity for cavity lengths (i.e. distance between the prisms) of <1.49 m. Since the beam strikes face $\overline{EF}$ at 45°, the effective focal length of the spherical surface is not the same in the vertical and horizontal directions. The beam within the cavity is therefore astigmatic. Ideally, the prisms would include an aspherical surface or two cylindrical surfaces, giving a non-astigmatic cavity beam. However, such surfaces are much more difficult to manufacture.
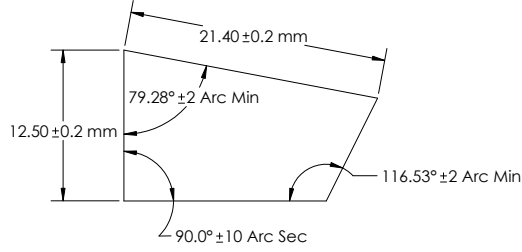
FIGURE 6.6. Dimensions of the $CaF_2$ prisms.

As observed with the $CaF_2$ windows, $CaF_2$ can be readily polished to surface roughness below 1 Å. However, superpolishing the prisms proved more difficult for manufacturers due to the more complicated prism geometry. White light interferometry was used to measure R.M.S. surface roughness between 2 and 2.4 Å. Since surface scatter loss scales as the square of roughness, this corresponds to a factor of $\sim 5$ increase in scatter loss.

6.3.2. PRISM CAVITY TESTING. Continuous-wave cavity ring-down spectroscopy was used to test the prism reflectivity at both 250 and 500 nm. Figure 6.7 shows the optical layout for the prism testing. The laser (Toptica, TA-FHG110) provided frequency doubled and quadrupled light at 500 and 250 nm respectively. An AOM was used to extinguish the light to the cavity once a resonance was detected. Mode matching the laser to the optical cavity is more complicated than for a typical dielectric mirror cavity due to astigmatic prism focusing. Mode matching was achieved with a series of four lenses. A 35 mm lens focused the beam into a 10 $\mu$m pinhole for spatial filtering. A 40 mm lens colimated the beam after the pinhole. Two 500 mm perpendicular cylindrical lenses matched the laser beam to the astigmatic cavity mode. Q-parameter theory was used to determine the needed distances between optics to match the $TEM_{0,0}$ laser mode to the $TEM_{0,0}$ mode of the cavity. The polarizer only allowed $p$-polarized light to reach the cavity. While $s$-polarized light would be quickly lost once the AOM turns off, it will also couple into the cavity much more strongly

than p-polarized and mask the p-polarized signal. Therefore, it was helpful to have a high
extinction ratio polarizer that is well aligned to $p$ prior to the cavity. The cavity length was
75 cm. The beam exiting the prism cavity was sent to a PMT for detection. Aligning the
prism cavity is not trivial and is outlined in detail by Lehmann et al.[68]
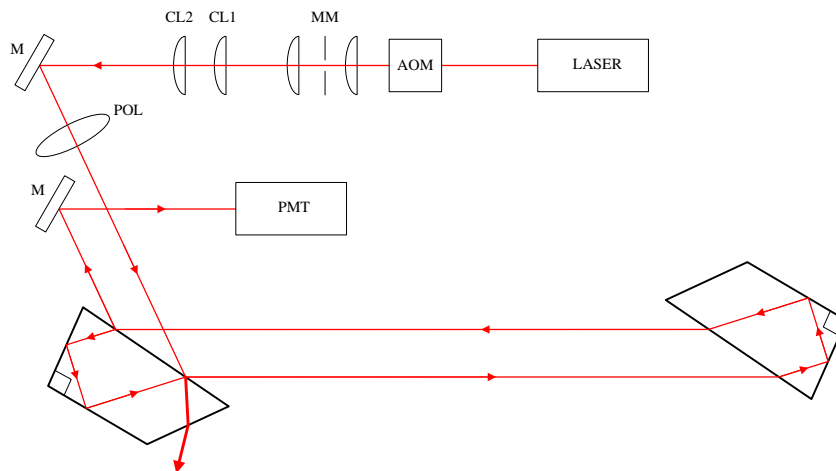


FIGURE 6.7. Optical schematic for cw-CRDS test of $CaF_2$ prisms. AOM:
acousto-optic modulator, MM: mode-match telescope, CL1: cylindrical lens 1,
oriented to focus vertically, CL2: cylindrical lens 2, oriented to focus horizon-
tally, POL: linear polarizer, M: steering mirror, PMT: photomultiplier tube

Cavity losses of 2500±100 and 400±100 ppm per pass were found at 250 nm and 500
nm respectively. The first prism (left prism in Fig. 6.1) has all planar surfaces and can
therefore be translated vertically a few mm without losing cavity finesse. The cavity loss
reported here was the minimum found after translating the first prism ±3 mm. These
losses include the loss of one prism and the loss incurred by the beam passing through 75
cm (the cavity length) of air. The loss contribution from ambient air was experimentally
measured. Subtracting the estimated loss in air from the cavity loss, one finds prism losses
of 1940±110 and 360±100 ppm at 250 nm and 500 nm respectively, which correspond to

prism reflectivities of 99.81±0.01% and 99.96±0.01% at 250 and 500 nm respectively. These findings are consistent with the estimated prism loss discussed in Sec. 6.2.2.

## 6.4. Conclusions and Implications to Electric Propulsion Diagnostics

We have demonstrated, to the best of our knowledge, the first use of $CaF_2$ for Brewster angle prism retroreflectors. Optical-loss measurements of <111> oriented $CaF_2$ windows showed prism reflectivities of ∼99.72% at 250 nm would be achievable with available manufacturing techniques. However, portions of the $CaF_2$ showed much higher loss, which was attributed to stress-induced birefringence. $CaF_2$ prisms were constructed with the <111> crystal axes closely aligned with the beam path. Prism reflectivities of 99.81±0.01% and 99.96±0.01% were found at 250 and 500 nm respectively. Not only do these prisms rival the best dielectric mirrors available for 250 nm, they also allow for high-finesse cavity operation simultaneously over hundreds of nm of optical bandwidth.

Several limitations in the prism performance were due to manufacturing difficulties, rather than physical limitations. For example, white light interferometry on $CaF_2$ showed surface roughness below 1 Å is readily achievable with superpolishing techniques. However, due to the more complicated prism geometry, polishing the prisms proved more difficult, resulting in a surface roughness of ∼2 Å. Therefore, the estimated surface scatter loss is ∼200 ppm at 250 nm, while improved polishing could yield scatter loss below ∼50 ppm. The remaining loss mechanisms contribute ∼1800 ppm of loss and are likely dominated by stress birefringence, which could be improved with lower birefringence $CaF_2$. Additionally, loss due to bulk absorption, bulk scatter, and birefringence are path-integrated effects and could be reduced with smaller prisms. Given that the spot size within the cavity is ∼400 $\mu$m, diffraction loss is negligible. The prism size, and therefore path-integrated loss, could be

scaled down by a factor of $\sim$5 or more without diffraction loss becoming significant. While such scaling would significantly reduce the prism loss, manufacturing becomes much more costly, and the prisms become more difficult to handle. Nevertheless, $CaF_2$ prisms with reflectivities above 99.95% at 250 nm should be physically achievable.

The application of such prisms which is most relevant to this thesis is the detection of sputtered boron in the plume of a Hall thruster. The boron CRDS sensor described in previous chapters utilized dielectric mirrors with $R \sim 99.75\%$ which is far below what can be achieved in other spectral regions and severely limits the optical sensitivity of the sensor. $CaF_2$ prisms provide the prospect of reducing the cavity loss, and therefore improve the detection sensitivity, by a factor of $\sim$5. Additionally, the dielectric mirrors used in the boron sensor are prone to degradation in the presence of the xenon plasma. One suspected cause of the degradation is damage induced by the vacuum ultraviolet radiation emitted by the thruster plasma. Given that $CaF_2$ is a commonly used material for deep-UV applications, the $CaF_2$ prisms should be much less susceptible to damage caused by the harsh plasma radiation.

As mentioned earlier, dielectric mirror reflectivity typically drops significantly when the wavelength deviates only a few percent from the central design wavelength. Prism retrore-flectors allow high-finesse cavity operation for hundreds of nm of bandwidth simultane-ously. $CaF_2$ prisms may enable simultaneous, high sensitivity detection of a number of UV-absorbent species which are relevant to electric propulsion. For example, singly, doubly, and triply charged xenon all have spectral lines near 250 nm. It is worth noting the xenon lines near 250 nm are not ground-state transitions, which would make quantifying xenon

number densities more difficult. Iron, which could be sputter eroded from the thruster anode, also absorbs in this spectral region.

# CHAPTER 7

# Summary and Conclusions

## 7.1. Summary

This thesis described the use of cavity ring-down spectroscopy (CRDS) to measure channel sputter erosion rates from the HiVHAc and SPT-70 Hall thrusters. Number densities of ground-state atomic boron were probed with light of wavelength near 250 nm within the plumes of the operating thrusters. The CRDS provided spatially-resolved measurements of the boron number density as a function of radius. As a complimentary measurement, laser-induced fluorescence (LIF) was used to measure boron speed distributions in the thruster plume. The product of the number density found by CRDS and mean axial boron speed found by LIF allowed for a total boron flux to be calculated from the channel. From the known density of the channel material, boron flux was related to volumetric channel erosion rate.

Changes to the sensor's hardware and operation improved the optical sensitivity compared to previous sensor version used by Tao and Yamamoto[44] and by Huang et al.[36] The optical sensitivity was improved by a factor of ~5 to $\sim 1.0 \times 10^{-8}$ cm$^{-1}$ Hz$^{-1/2}$, which improved the signal to noise ratio of boron detection and decreased the needed time to acquire spectra. Degradation of the cavity mirrors when exposed to the thruster plasma remains a problem but has been significantly mitigated by increasing the system data acquisition rate and including a purge flow in front of the cavity mirrors. Optical sensitivity was decreased by a factor of ~2 after 11 hours of thruster measurements.

Channel erosion rates of the NASA High Voltage Hall Accelerator (HiVHAc) thruster were measured at eight different operating points with discharge voltages ranging from 330

to 500 V and discharge powers from 1 to 3 kW. Channel erosion rates varied from $5 \times 10^{-12}$ to $8 \times 10^{-12}$ m$^3$/s. The erosion rate trend was found to be proportional to discharge power, which is consistent with the optical-emission spectroscopy work by Williams et al.[25] The NASA 300M and 457M thrusters[25], and H6 thruster[36] were found to erode at a rate proportional to $I_d \times V_d^2$.

The channel erosion rate of the SPT-70 thruster was found to be $2.27 \pm 0.21 \times 10^{-13}$ and $2.47 \pm 0.020 \times 10^{-13}$ m$^3$/s at 275 and 300 V discharge voltage respectively. The SPT-70 is only designed to have one nominal operating condition, and a parametric erosion study was not possible. However, the two erosion rates measured were also found to be proportional to the discharge voltage. The channel erosion rate was also measured using profilometry, and found to be a factor of $\sim 5$ higher than that estimated by the CRDS sensor. Possible systematic errors were discussed.

Laser-induced fluorescence was used to measure axial boron speed distributions in the SPT-70 thruster plume. To the best of the author's knowledge, the measurements were the first of their kind. Boron speed distributions were measured at two of the same locations for which CRDS number density measurements had been obtained. The measured speed distribution did not vary significantly between the two locations measured. The mean boron speed, which was used to compute the boron flux, was found to be $3840 \pm 180$ m/s.

The design, construction and characterization of calcium fluoride prism retroreflectors was also presented. The CRDS sensor used in these measurements employed dielectric coating mirrors which have relatively poor performance in the ultraviolet region. CaF$_2$ prism retroreflectors show promise to improve both the bandwidth and peak finesse of optical cavities in the ultraviolet region. Prior to prism construction, optical loss measurements of CaF$_2$

windows were performed to help estimate prism performance. Prisms were constructed and found to have a reflectivity of $99.81 \pm 0.01\%$ and $99.96 \pm 0.01\%$ at 250 and 500 nm respectively. Various improvements are suggested which could reasonably allow prism reflectivities of 99.95%.

## 7.2. Future Work

7.2.1. Further Sensor Improvements. The erosion sensor described in this work has demonstrated the ability to detect boron erosion from even relatively small thrusters and is sufficiently robust for extended periods of data acquisition. However, the sensor underestimates the erosion rate, which warrants further investigation of systematic errors. Two likely causes for the discrepancy were discussed. First, the sensor assumes boron is sputtered as atoms, for which there is evidence from boron nitride channels. However, to the best of the author's knowledge, there is no such evidence for the SPT-70 channel material. Measurement of the sputtered species composition would be useful, perhaps using a residual gas analyzer. The second proposed systematic error is that not all of the sputtered boron exits the channel and is therefore not counted by the erosion sensor. High-fidelity thruster erosion models (i.e. a highly detailed model) may be able to provide estimates of the fraction of boron which exits the channel.

Also, the CRDS sensor only measures ground-state neutral boron. Any excited or ionized boron will not be counted causing underestimation of the erosion rate. Estimates of the population fraction which is ionized have been made, however, higher fidelity models may prove to be more informative and accurate. In the case of the HiVHAc thruster, no plasma diagnostics have yet been performed within the channel, and electron temperatures and

plasma densities had to be roughly estimated. Models of electronic excitation will also be helpful in estimating what fraction of the boron population is counted by the sensor.

7.2.2. FUTURE THRUSTER EROSION STUDIES. Recent advances in Hall thrusters have shown promise to reduce channel erosion rates by a factor of ~100 to 1000 via magnetic shielding.[76] In magnetic shielding, the thruster channel is chamfered near the exit plane, and the magnetic field topology is altered such that the magnetic field lines follow more parallel to the channel wall as opposed to perpendicular to it. The electron temperatures near the channel wall are much lower, resulting in a lower potential drop through the sheath, and therefore, lower ion-impact energies at the wall. Also, ions must cross magnetic fields lines to reach the wall, and the flux of ions to the wall is greatly reduced. Magnetic shielding of thrusters is a great advancement of Hall thruster technology and may prove to be 'game changing'. However, magnetically shielded thrusters are still in the developmental stage. All Hall thrusters that have been flown, are qualified to fly, or are in the flight-qualification process do not employ magnetic shielding. As such, the erosion diagnostics discussed in this thesis are still relevant.

The most likely future application for the CRDS erosion sensor is as a diagnostic tool for the thruster flight qualification process. Prior to a Hall thruster being flown in space, both its performance and lifetime need to be thoroughly characterized at all intended throttle points. Given the cost associated with premature thruster failure, it is unlikely that CRDS will replace long-duration tests entirely. However, performing a long-duration test at all desired thruster operating conditions can also be cost prohibitive. The role of the CRDS sensor will be to provide information about the channel erosion rate for the operating conditions not

tested in the long-duration tests. Several corporations which develop flight Hall thrusters have expressed interest in such measurements.

7.2.3. FUTURE CALCIUM FLUORIDE PRISM WORK. Calcium fluoride prisms were developed as a means to provide broadband and high-finesse optical cavities in the ultraviolet region. The prism reflectivity is roughly equal to that of the best available dielectric mirrors at 250 nm. Cavity ring-down spectroscopy, which was used to characterize the prisms, only gives the sum of all the losses within the cavity. While estimates of the various loss mechanisms were made, it is difficult to decouple all loss mechanisms. Johnston et al. measured fused silica prism retroreflector performance at many wavelengths ($\sim$20) and used the fit to a loss model to accurately estimate the contribution of each loss mechanism.[69] Similar measurements are planned for the $CaF_2$ prisms and should provide significant information the the prism performance. Even in the absence of such measurements, it seems clear the $CaF_2$ prism performance is limited mostly by path-integrated effects such as birefringence and bulk scatter. These effects can be reduced by decreasing the size of the prisms, however, at greatly increased manufacturing cost and difficulty in handling.

# Bibliography

[1] D. Goebel and I. Katz, *Fundamentals of Electric Propulsion: Ion and Hall Thrusters.* Wiley, 2008.

[2] "Nasa advanced space transportation program." http://www.nasa.gov. last access: 17 February, 2014.

[3] D. Mazanek, J. Brophy, and R. Merrill, "Asteroid retrieval mission concept - trailblazing our future in space and helping to protect us from earth impactors," in $3^{rd}$ *IAA Planetary Defense Conference*, (Flagstaff, AZ), pp. IAA–PDC13–04–14, April 2013.

[4] R. Goddard, 1920.

[5] R. H. Goddard, "The green notebooks, vol. 1." The Dr. Robert H. Goddard Collection at the Clark University Archives, Clark University, Worchester, Massachusetts.

[6] E. Y. Choueiri, "A critical history of electric propulsion: The first 50 years (1906-1956)," *Journal of Propulsion and Power*, vol. 20, pp. 193–203, Mar. 2004.

[7] "Nasa next thruster." http://www.nasa.gov. last access: 13 February, 2014.

[8] P. Wilbur, "Limits on high specific impulse ion thruster operation," in *Joint Propulsion Conferences*, pp. AIAA–2004–3818, American Institute of Aeronautics and Astronautics, July 2004.

[9] V. V. Zhurin, H. R. Kaufman, and R. S. Robinson, "Physics of closed drift thrusters," *Plasma Sources Science and Technology*, vol. 8, no. 1, p. R1, 1999.

[10] A. Anders, ed., *Handbook of Plasma Immersion Ion Implantation and Deposition.* Wiley-Interscience, 2000.

[11] H. Bach and D. Krause, eds., *Thin Films on Glass.* Springer, 2003.

[12] C. C. Farnell, *Performance and Liftume Simulation of Ion Thruster Optics.* PhD thesis, Colorado State University, 2007.

[13] I. Langmuir, "Positive Ion Currents from the Positive Column of Mercury Arcs," *Science*, vol. 58, pp. 290–291, Oct. 1923.

[14] M. Gamero-Castano and I. Katz, "Estimation of hall thruster erosion using hphal," in $29^{th}$ *International Electric Propulsion Conference*, (Princeton University), pp. IEPC–2005–303, 2005.

[15] B. Rubin, J. L. Topper, and A. P. Yalin, "Total and differential sputter yields of boron nitride measured by quartz crystal microbalance," *Journal of Physics D: Applied Physics*, vol. 42, p. 205205, Oct. 2009.

[16] K. D. Grys, A. Mathers, B. Welander, and V. Khayms, "Demonstration of 10,400 Hours of Operation on 4.5 kW Qualification Model Hall Thruster," in *46TH AIAA/ASME/SAE/ASEE JOINT PROPULSION CONFERENCE & EXHIBIT*, no. AIAA-2010-6698, (Nashville, TN), 2010.

[17] R. Shastry, D. Herman, G. Soulas, and M. Patterson, "NASA's Evolutionary Xenon Thruster (NEXT) Long-Duration Test as of 736 kg of Propellant Throughput," in *48th AIAA/ASME/SAE/ASEE Joint Propulsion Conference & Exhibit*, no. AIAA-2012-4023, (Atlanta, Georgia), 2012.

[18] P. Y. Peterson and D. H. Manzella, "Investigation of the Erosion Characteristics of a Laboratory Hall Thruster," in *39th AIAA/ASME/SAE/ASEE Joint Propulsion Conference & Exhibit*, no. AIAA-2003-5005, (Huntsville, Alabama), 2003.

[19] T. Misuri, A. Milani, and M. Andrenucci, "Development of a Telemicroscopy Diagnostic Apparatus and Erosion Modelling in Hall Effect Thrusters," in *31st International Electric Propulsion Conference*, no. IEPC-2009-036, (Ann Arbor, Michigan), 2009.

[20] Y. Garnier, V. Viel, J.-F. Roussel, and J. Bernard, "Low-energy xenon ion sputtering of ceramics investigated for stationary plasma thrusters," *Journal of Vacuum Science & Technology A: Vacuum, Surfaces, and Films*, vol. 17, no. 6, p. 3246, 1999.

[21] A. P. Yalin, V. Surla, C. Farnell, M. Butweiller, and J. D. Williams, "Sputtering Studies of Multi-Component Materials by Weight Loss and Cavity Ring-Down Spectroscop," in *42nd AIAA/ASME/SAE/ASEE Joint Propulsion Conference & Exhibit*, no. AIAA-2006-4338, (Sacramento, California), 2006.

[22] B. Rubin, J. L. Topper, and a. P. Yalin, "Total and differential sputter yields of boron nitride measured by quartz crystal microbalance," in *30th International Electric Propulsion Conference*, no. IEPC-2007-074, (Florence, Italy), 2007.

[23] D. Pagnon, L. Balika, and S. Pellerin, "QCM and OES: two ways used to study simultaneously HET thruster chamber ceramic erosion. First QCM results on PPS100-ML validate previous OES measurements.," in *31st International Electric Propulsion Conference*, no. IEPC-2009-118, (Ann Arbor, Michigan), 2009.

[24] S. Cho, S. Yokota, K. Hara, D. Takahashi, Y. Arakawa, K. Komurasaki, and A. Kobayashi, "Hall Thruster Channel Wall Erosion Rate Measurement Method Using Multilayer Coating Chip," in *46th AIAA/ASME/SAE/ASEE Joint Propulsion Conference & Exhibit*, no. AIAA-2010-6697, (Nashville, TN), 2010.

[25] G. Williams, G. Soulas, and H. Kamhawi, "Optical diagnostic characterization of high-power hall thruster wear and operation," in *Joint Propulsion Conferences*, pp. –, American Institute of Aeronautics and Astronautics, July 2012.

[26] M. Celik, O. Batishchev, and M. Martinez-Sanchez, "Use of emission spectroscopy for real-time assessment of relative wall erosion rate of BHT-200 hall thruster for various regimes of operation," *Vacuum*, vol. 84, pp. 1085–1091, Apr. 2010.

[27] W. a. Hargus and J. Strafaccia, "Optical Boron Nitride Insulator Erosion Characterization of a 200 W Xenon Hall Thruster," in *41st AIAA/ASME/SAE/ASEE Joint Propulsion Conference*, p. 3529, 2005.

[28] K. Busch and M. Busch, *Cavity-Ringdown Spectroscopy (ACS Symposium Series 720)*. Oxford University Press, 1999.

[29] G. Berden, R. Peeters, and G. Meijer, "Cavity ring-down spectroscopy: Experimental schemes and applications," *International Reviews in Physical Chemistry*, vol. 19, no. 4, pp. 565–607, 2000.

[30] G. Berden and R. Engeln, eds., *Cavity Ring-Down Spectroscopy: Techniques and Applications*. Wiley-Blackwell, 2009.

[31] G. Gagliardi and H. Loock, eds., *Cavity-Enhanced Spectroscopy and Sensing*. Springer Series in Optical Sciences, 2014.

[32] A. Yalin, V. Surla, M. Butweiller, and J. Williams, "Detection of sputtered metals with cavity ring-down spectroscopy," *Appl. Opt.*, vol. 44, pp. 6496–6505, Oct. 2005.

[33] V. Surla, P. J. Wilbur, M. Johnson, J. D. Williams, and a. P. Yalin, "Sputter erosion measurements of titanium and molybdenum by cavity ring-down spectroscopy," *Review of Scientific Instruments*, vol. 75, no. 9, p. 3025, 2004.

[34] L. Tao, A. P. Yalin, and N. Yamamoto, "Cavity ring-down spectroscopy sensor for ion beam etch monitoring and end-point detection of multilayer structures.," *The Review of scientific instruments*, vol. 79, p. 115107, Nov. 2008.

[35] N. Yamamoto, L. Tao, B. Rubin, J. D. Williams, and A. P. Yalin, "Sputter Erosion Sensor for Anode Layer-Type Hall Thrusters Using Cavity Ring-Down Spectroscopy," *Journal of Propulsion and Power*, vol. 26, pp. 142–148, Jan. 2010.

[36] W. Huang, A. Galimore, T. Smith, L. Tao, and A. Yalin, "Initial cavity ring-down density measurement on a 6-kw hall thruster," in *Joint Propulsion Conferences*, pp. –, American Institute of Aeronautics and Astronautics, July 2011.

[37] W. Huang, A. D. Gallimore, and T. B. Smith, "The Technical Challenges of using Cavity Ring-Down Spectroscopy to Study Hall Thruster Channel Erosion," in *32nd International Electric Propulsion Conference*, no. IEPC-2011-030, (Wiesbaden, Germany), 2011.

[38] Y. Sakamoto, K. Tanaka, T. Asakawa, and K. Tonokura, "Wavelength Modulation Spectroscopy Detection of $N_2O$ Using a Direct-Bonded Quasi-Phase-Matched $LiNbO_3$-Ridge-Waveguide Mid-Infrared Laser," *Japanese Journal of Applied Physics*, vol. 50, p. 062401, June 2011.

[39] C. J. Dasch, "One-dimensional tomography: a comparison of Abel, onion-peeling, and filtered backprojection methods.," *Applied optics*, vol. 31, pp. 1146–52, Mar. 1992.

[40] S. Mazouffre, P. Echegut, and M. Dudeck, "A calibrated infrared imaging study on the steady state thermal behaviour of hall effect thrusters," *Plasma Sources Science and Technology*, vol. 16, no. 1, p. 13, 2007.

[41] G. Betz, "Electronic Excitation in Sputtered Atoms and the Oxygen Effect," *Nuclear Instruments and Methods in Physics Research B*, vol. 27, no. 1, pp. 104–118, 1987.

[42] J. Booth, G. Cunge, L. Biennier, D. Romanini, and A. Kachanov, "Ultraviolet cavity ring-down spectroscopy of free radicals in etching plasmas," *Chemical Physics Letters*, vol. 317, no. 6, pp. 631 – 636, 2000.

[43] A. Schwabedissen, A. Brockhaus, A. Georg, and J. Engemann, "Determination of the gas-phase si atom density in radio frequency discharges by means of cavity ring-down spectroscopy," *Journal of Physics D: Applied Physics*, vol. 34, no. 7, p. 1116, 2001.

[44] N. Yamamoto, A. P. Yalin, L. Tao, T. B. Smith, A. D. Gallimore, and Y. Arakawa, "Development of Real-time Boron Nitride Erosion Monitoring System for Hall Thrusters by Cavity Ring-Down Spectroscopy," *Transactions of Space Technology Japan*, vol. 7, pp. 1–6, 2009.

[45] P. Werle, R. Mucke, and F. Slemr, "The limits of signal averaging in atmospheric trace-gas monitoring by tunable diode-laser absorption spectroscopy (tdlas)," *Applied Physics B*, vol. 57, no. 2, pp. 131–139, 1993.

[46] H. Huang and K. K. Lehmann, "Noise caused by a finite extinction ratio of the light modulator in CW cavity ring-down spectroscopy," *Applied Physics B*, vol. 94, pp. 355–366, Nov. 2008.

[47] B. C. Lee, L. Tao, J. M. Taylor, and A. P. Yalin, "Sensitivity Improvements to Laser Sensor for Boron Nitride Erosion in Hall Thrusters," in *32nd International Electric Propulsion Conference*, p. 068, 2011.

[48] J. W. Dankanich, H. Kamhawi, and A. J. Mathers, "Hivhac maximum operating power mission impacts," in $31^{st}$ *International Electric Propulsion Conference*, (Ann Arbor, MI,), pp. IEPC–2009–213, September 2009.

[49] K. H., P. L. Manzella D., and H. T., "In-space propulsion high voltage hall accelerator development project overview," in $46^{th}$ *AIAA/ASME/SAE/ASEE Joint Propulsion Conference & Exhibit*, (Nashville, TN), pp. AIAA 2010–6860, July 2010.

[50] H. Kogelnik and T. Li, "Laser beams and resonators," *Appl. Opt.*, vol. 5, pp. 1550–1567, Oct 1966.

[51] J. E. Flad, S. S. Brown, J. B. Burkholder, H. Stark, and A. R. Ravishankara, "Absorption cross sections for the $\tilde{A}\ ^2A''$ $(0,9^0,0) \leftarrow \tilde{X}\ ^2A'$ $(0,0^1,0)$ band of the HCO radical," *Phys. Chem. Chem. Phys.*, vol. 8, pp. 3636–3642, 2006.

[52] L. Tao, A. Yalin, and F. Collins, "Velocity Profiles of Boron Atoms Sputtered from Boron Nitride by Low Energy Xenon Ions," in *32nd International Electric Propulsion Conference*, no. IEPC-2011-067, (Wiesbaden, Germany), 2011.

[53] G. Betz and K. Wien, "Energy and angular distributions of sputtered particles," *International Journal of Mass Spectrometry and Ion Processes*, vol. 140, no. 1, pp. 1 – 110, 1994.

[54] M. Gryzinski, "Classical theory of atomic collisions. i. theory of inelastic collisions," *Phys. Rev.*, vol. 138, pp. A336–A358, Apr 1965.

[55] B. D. Smith, I. D. Boyd, H. Kamhawi, and W. Huang, "Hybrid-pic modeling of a high-voltage, high-specific-impulse hall thruster," in *Joint Propulsion Conferences*, pp. –, American Institute of Aeronautics and Astronautics, July 2013.

[56] A. Kramida, Yu. Ralchenko, J. Reader, and and NIST ASD Team. NIST Atomic Spectra Database (ver. 5.1), [Online]. Available: `http://physics.nist.gov/asd` [2013, September 18]. National Institute of Standards and Technology, Gaithersburg, MD., 2013.

[57] A. Morozov, "The conceptual development of stationary plasma thrusters," *Plasma Physics Reports*, vol. 29, no. 3, pp. 235–250, 2003.

[58] J. Fife and M. Martinez-Sanchez, "Characterization of the spt-70 plume using electrostatic probes," in *Joint Propulsion Conferences*, pp. –, American Institute of Aeronautics and Astronautics, July 1998.

[59] J. T. Yim, *Computational Modeling of Hall Thruster Channel Wall Erosion*. PhD thesis, University of Michigan, 2008.

[60] S. K. Absalamov, V. B. Andreev, T. Colbert, M. Day, V. V. Egorov, R. U. Gnizdor, H. Kaufman, V. Kim, A. I. Koriakin, and K. N. Kozubskii, "Measurement of plasma parameters in the stationary plasma thruster (SPT-100) plume and its effect on spacecraft components," in *Joint Propulsion Conference and Exhibit* (S. K. Absalamov, V. B. Andreev, T. Colbert, M. Day, V. V. Egorov, R. U. Gnizdor, H. Kaufman, V. Kim, A. I. Koriakin, and K. N. Kozubskii, eds.), July 1992.

[61] A. Ahebo, A. Anton, I. Garmendia, and I. Caro, "Simulation of wall erosion in hall thrusters," in *30th International Electric Propulsion Conference*, (Florence, Italy), pp. IEPC–2007–067, 2007.

[62] R. Cedolin, W. Hargus Jr., P. Storm, R. Hanson, and M. Cappelli, "Laser-induced fluorescence study of a xenon hall thruster," *Applied Physics B*, vol. 65, no. 4-5, pp. 459–469, 1997.

[63] W. Hargus, Jr. and M. Cappelli, "Laser-induced fluorescence measurements of velocity within a hall discharge," *Applied Physics B*, vol. 72, no. 8, pp. 961–969, 2001.

[64] D. H. Wensheng Huang, *Study of Hall Thruster Discharge Channel Wall Erosion via Optical Diagnostics.* PhD thesis, University of Michigan, 2011.

[65] G. J. Williams, *The use of laser-induced fluorescence to characterize discharge cathode erosion in a 30 cm ring-cusp ion thruster.* PhD thesis, University of Michigan, 2000.

[66] R. C. Hilborn, "Einstein coefficients, cross sections, f values, dipole moments, and all that," *American Journal of Physics*, vol. 50, pp. 982–986, Nov. 1982.

[67] H. Moosmüller, "Brewster's angle porro prism: A different use for a pellin-broca prism," *Appl. Opt.*, vol. 37, pp. 8140–8142, Dec 1998.

[68] K. K. Lehmann, P. S. Johnston, and P. Rabinowitz, "Brewster angle prism retroreflectors for cavity enhanced spectroscopy," *Appl. Opt.*, vol. 48, pp. 2966–2978, Jun 2009.

[69] P. S. Johnston and K. K. Lehmann, "Cavity enhanced absorption spectroscopy using abroadband prism cavity and a supercontinuum source," *Opt. Express*, vol. 16, pp. 15013–15023, Sep 2008.

[70] "Tiger optics." www.tigeroptics.com. last access: 1 January, 2014.

[71] H. Chen and W. B. Yan, "Prism-based cavity ring-down spectroscopy: Broadband and ultrahigh reflectivity," in *62nd International Symposium on Molecular Spectroscopy*, 2007.

[72] S. Logunov and S. Kuchinsky, "Experimental and theoretical study of bulk light scattering in $CaF_2$ monocrystals," *Journal of Applied Physics*, vol. 98, p. 053501, Sept. 2005.

[73] A. C. R. Pipino, J. W. Hudgens, and R. E. Huie, "Evanescent wave cavity ring-down spectroscopy with a total-internal-reflection minicavity," *Review of Scientific Instruments*, vol. 68, pp. 2978–2989, Aug 1997.

[74] J. H. Burnett, Z. H. Levine, and E. L. Shirley, "Intrinsic birefringence in calcium fluoride and barium fluoride," *Physical Review B*, vol. 64, no. 24, p. 241102, 2001.

[75] J. H. Burnett, "Stress-optical coefficients of 157 nm materials," in *SEMATECH 157nm Technical Data Review*, 2011.

[76] I. Mikellides, I. Katz, R. Hofer, D. Goebel, K. de Grys, and A. Mathers, "Magnetic shielding of the acceleration channel walls in a long-life hall thruster," in *Joint Propulsion Conferences*, pp. –, American Institute of Aeronautics and Astronautics, July 2010.